# Investigation of the effect of morphological and crystallographic textures on the ductility limits of thin metal sheets using a CPFEM-based approach

S. Zhou, M. Ben Bettaieb *, F. Abed-Meraim

*Université de Lorraine, CNRS, Arts et Métiers Institute of Technology, LEM3, F-57070 Metz, France*
*DAMAS, Laboratory of Excellence on Design of Alloy Metals for low-mAss Structures, Université de Lorraine, France*

*Keywords:*
Ductility
Microstructures
Crystal plasticity
Finite strain
Stability and bifurcation

A B S T R A C T

The current contribution investigates the effect of some relevant microstructural parameters (specifically, morphological and crystallographic textures) on the ductility limits of polycrystalline aggregates using the Crystal Plasticity Finite Element Method (CPFEM). The polycrystalline aggregates are assumed to be representative of thin metal sheets and their macroscopic behavior is determined from that of their constituent single crystals on the basis of the periodic homogenization technique. The single crystal behavior is described by a finite strain elastoplastic framework in which the plastic flow rule obeys the classical Schmid law and plastic deformation is solely attributed to the slip on the crystallographic slip systems. The CPFEM is implemented within and in connection with ABAQUS/Standard finite element code. The ductility limits are predicted by the Rice bifurcation theory where strain localization is detected when the macroscopic acoustic tensor becomes singular. Three grain morphologies (namely, cube, random, and elongated morphology) and three initial crystallographic textures (namely, cube, random, and copper orientation) are considered to investigate the effect of morphological and crystallographic textures on the onset of plastic strain localization. The numerical results indicate that the effect of initial crystallographic texture is much more pronounced than that of grain morphology on the predicted ductility limits. In addition, the impact of grain size and sheet thickness are thoroughly analyzed. The research reveals that the trends of the predicted ductility limits are strongly dependent on the size effects.

## 1. Introduction

The ultimate goal of designers and producers of new metal alloys is to improve the mechanical properties of industrial devices and components (strength, ductility, creep resistance, etc.). This improvement necessitates a thorough understanding of the physical and microstructural factors that influence these mechanical properties. In this context, the investigation of the effect of microstructural parameters on the mechanical behavior in general and specifically on the ductility limit of thin metal sheets has received an increasing interest in the last few decades. To this end, several theoretical predictive tools have been developed in the past to numerically determine the ductility limits following the concept of forming limit diagrams (FLDs), which has been first introduced by Keeler and Backhofen (1963) and Goodwin (1968). The development of such predictive tools is based on the combination of a constitutive framework describing the evolution of mechanical variables during plastic deformation with a localized necking criterion. Constitutive frameworks are classically categorized into two main families: phenomenological and multiscale frameworks.

Phenomenological models have been widely used to analyze the effect of several mechanical features on the onset of localized necking. In this field, Ben Bettaieb and Abed-Meraim (2015) have demonstrated that the predicted formability limit strains increase with the isotropic hardening exponent. This result is valid for all of the strain paths that compose the FLD (ranging from uniaxial to equibiaxial tension states). In the latter investigation, a rate-independent constitutive framework with isotropic hardening and isotropic plasticity has been adopted to describe the metal sheet mechanical behavior. The effect of plastic anisotropy on the predicted ductility limit strains has been analyzed in Barlat (1987), where the author has demonstrated that plastic anisotropy parameters impact the limit strains essentially for biaxial strain paths (especially near equibiaxial strain state). More recently, the effect of the sensitivity of the mechanical behavior to the strain rate on the predicted ductility limit strains has been explored in Ben Bettaieb and Abed-Meraim (2017b). In this reference, the authors have demonstrated that the strain-rate sensitivity significantly delays the onset of localized necking for all the strain paths. The numerical approach developed in Ben Bettaieb and Abed-Meraim (2015) has been extended

* Corresponding author at: Université de Lorraine, CNRS, Arts et Métiers Institute of Technology, LEM3, F-57070 Metz, France.
*E-mail address:* Mohamed.BenBettaieb@ensam.eu (M. Ben Bettaieb).

https://doi.org/10.1016/j.euromechsol.2024.105293

in Ben Bettaieb and Abed-Meraim (2017a) to include kinematic hardening in the constitutive modeling. On the basis of this extension, the authors have shown that the consideration of kinematic hardening lowers the predicted ductility limit strains. Despite their wide use to model the mechanical behavior in general and to predict the ductility limits in particular, classical phenomenological frameworks are often unable to appropriately take into account some specific mechanical and microstructural properties, such as the evolution of grain morphology and crystallographic texture induced by plastic deformation, and grain size effects. As a result, a new generation of phenomenological frameworks has recently been developed to better consider these aspects. In this context, the impact of grain size has been considered by incorporating Hall–Petch effects into the FLD predictions (Xu et al., 2015; Butuc et al., 2021). It has been demonstrated in the above-cited contributions that as the grain size increases, the mean ductility decreases. In addition, when the sheet thickness decreases, a substantial scatter of ductility is observed. The effect of crystallographic texture evolution on the incipience and development of localized necking has been studied by incorporating distortional hardening into phenomenological modeling as proposed in Manopulo et al. (2015) and Jeong et al. (2017). More recently, Jedidi et al. (2020) have used an enhanced two-surface constitutive model to describe the mechanical behavior and to investigate the ductility limit of hexagonal closed packed (HCP) sheet metals. This model enables to explicitly predict, in a phenomenological way, plastic deformation due to the activation of slip and twinning deformation modes. Such a model can be viewed as an intermediate approach between classical phenomenological and multiscale models.

Unfortunately, despite the substantial advancements made in phenomenological modeling, the resulting models most often remain unable to adequately capture the influence of the above-mentioned microstructural phenomena on the formability predictions. To overcome these major limitations, several multiscale schemes have been adopted for the prediction of the ductility limits of thin metal sheets. Within these multiscale frameworks, the mechanical behavior is explicitly modeled at the microscopic scale (which corresponds generally to the single crystal scale), and some relevant scale-transition rules are used to derive the macroscopic behavior from that of the microscopic constituents. Multiscale schemes used to predict the macroscopic behavior of polycrystalline aggregates are classically categorized into two families: mean-field and full-field schemes. The full-constraint Taylor scheme is one of the most widely used mean-field schemes in the literature. Due to its simplicity, this scale-transition scheme has been frequently used for predicting FLDs within the framework of elastoplasticity (Knockaert et al., 2002; Yoshida and Kuroda, 2012), rigid viscoplasticity (Inal et al., 2005; Gupta et al., 2018), and elastoviscoplasticity (Lévesque et al., 2010). The use of the multiscale Taylor model in these investigations offers several practical benefits. For instance, the strain homogeneity assumption adopted in this model allows significantly simplifying the numerical implementation, thus leading to considerable reduction in CPU time (compared to other multiscale schemes). In addition, the Taylor scale-transition scheme enables to accurately predict the evolution of crystallographic textures during plastic deformation. On the other hand, the full-constraint Taylor model presents several conceptual drawbacks: the equilibrium condition at the grain level is not fulfilled, the grain morphology is not always accurately described as only the grain weight is considered in this scale-transition rule, and the interactions between each grain and its surrounding medium are not accounted for. To overcome some of these limitations, the self-consistent mean-field multiscale scheme has been used in the literature to predict the ductility limits of thin metal sheets. This multiscale scheme has been combined with rate-dependent (Signorelli et al., 2009; Schwindt et al., 2015) and rate-independent (Franz et al., 2013; Akpama et al., 2017) crystal plasticity constitutive frameworks to model the polycrystalline mechanical behavior and then to predict the ductility limits. Unlike the Taylor model, the self-consistent approach allows the fulfillment of the equilibrium state at the polycrystalline scale and better accounting for the grain morphology, as each grain is assumed to be ellipsoidal. Hence, the grain morphology is described by the weight and the half-axes of the corresponding ellipsoid. Despite these undeniable advances, mean-field multiscale techniques still remain often limited when used to model the polycrystalline behavior and to predict the onset of localized necking of new materials with complex microstructural properties. Indeed, mean-field schemes are for instance unable to predict local strain and stress fields developed in a single grain. This may result in large fluctuation of the local mechanical variables for strongly anisotropic crystals. Furthermore, the statistical analysis of the microstructures does not allow for the evaluation of the effect of the real grain shape as well as the details of the grain spatial distributions. Consequently, full-field multiscale schemes have recently been designed and used to accurately relate the microstructural state to the macroscopic mechanical response and then to efficiently predict the formability limits. In fact, full-field multiscale schemes are able to accurately take into account realistic grain morphologies using the Voronoi tessellation technique (Amelirad and Assempour, 2019; Chaugule and le Graverend, 2022; Onimus et al., 2022). Furthermore, full-field approaches allow taking into account the strain heterogeneity within the grain, which arises from the collective motions of dislocations, as well as realistic boundary conditions that accurately describe both geometrical anisotropy and deformation induced anisotropy (such as periodic boundary conditions). These full-field schemes are based on the Crystal Plasticity Finite Element Method (CPFEM), such as in Kim et al. (2017), Amelirad and Assempour (2019) and Tran et al. (2022), or on the Crystal Plasticity Fast Fourier Transform technique (CPFFT), as in Nagra et al. (2018, 2020). In all of the above cited references based on the CPFEM or CPFFT approaches, only rate-dependent crystal plasticity models are used to simulate the behavior of single crystals. Furthermore, the initial imperfection approach (Marciniak and Kuczyński, 1967) is mostly used to predict the ductility limits (with the exception of Amelirad and Assempour (2019), who have used a stress concentration criterion to predict the onset of localized necking). In Kim et al. (2017), the numerical approach based on the coupling of the CPFEM to the initial imperfection approach has been used to predict the ductility limits of a ferritic stainless steel. The influence of slip system activity on the yield criteria and forming limits has been discussed. In Amelirad and Assempour (2019), the effect of the grain size on the forming limits of stainless steel 316 L sheets has been explored. It has been illustrated through this research that the forming limit diagrams shift down with decreasing the average grain size. In Tran et al. (2022), the size effect on the formability of ultra-thin metallic bipolar plate for proton exchange membrane (PEM) fuel cell has been investigated. The results of this investigation reveal a significant degradation of the formability of the ultra-thin FSS sheet as the thickness-to-grain size ratio decreases. In Nagra et al. (2018), the CPFFT method has been coupled with the initial imperfection approach to predict the FLDs of AA5754 and AA3003 aluminum alloys. The results obtained by the CPFFT approach have been compared with those predicted by the well-known Taylor multiscale scheme. Furthermore, the effects of various grain shapes as well as local grain interactions on the FLD predictions have been studied. The study reveals that among the various microstructural features, the grain morphology has the strongest effect on the predicted FLDs, which can significantly be improved if the actual grain structure of the material is properly accounted for in the numerical models. The approach developed by Nagra et al. (2018) has recently been extended by Nagra et al. (2020) to predict dynamic recrystallization (DRX) and formability of HCP metals, such as magnesium alloys at warm temperature. This study indicates that DRX has a significant impact on the deformed grain structure, grain size and texture evolution and also highlights the importance of accounting for DRX during FLD simulations at high temperature.

In the present contribution, a polycrystalline aggregate is selected as Representative Volume Element (RVE) of the studied thin metal sheet. The selection of such an aggregate and its size should fulfill the

principle of separation of the length scales: the scale of the microstructural fluctuations must be smaller than the scale of the RVE, which should be again much smaller than the macroscopic field fluctuations. A CPFEM-based multiscale scheme is used to model the mechanical behavior of the RVE. This scheme is based on the periodic homogenization technique (Ben Bettaieb et al., 2012; Zhu et al., 2020a,b, 2023), which allows accurately reproducing the periodic arrangement of the crystallographic structure. Due to its small thickness, only one representative volume element (called also unit cell in the context of periodic homogenization approach) is considered through the sheet thickness direction. This unit cell generates the thin metal sheet by periodicity in the two geometric plane directions. To be consistent with classical FLD predictions, the macroscopic plane stress assumption is used in the direction normal to the sheet plane. Hence, periodic boundary conditions are applied only in the two plane directions. To automatically apply these boundary conditions and the macroscopic loading on the polycrystalline aggregate, we have used the set of Python scripts HOMTOOLS developed by Lejeunes and Bourgeois (2011). The periodic homogenization equations are solved by the finite element method (ABAQUS, 2014) after spatial discretization of the unit cell. A single crystal is assigned at each integration point of the finite element mesh. Unlike previous contributions based on a rate-dependent formulation (Kim et al., 2017; Nagra et al., 2018; Amelirad and Assempour, 2019; Nagra et al., 2020; Tran et al., 2022), the single crystal constitutive equations follow a finite strain rate-independent constitutive framework. Within this constitutive framework, the plastic flow, which is assumed to be solely due to the shear over the slip systems, is modeled by the classical Schmid law (Schmid and Boas, 1935). This rate-independent formulation is more appropriate when the viscous effects are negligible, which is typically the case in cold forming processes. Furthermore, rate-dependent single crystal equations are highly non-linear (due to the small values of the strain-rate sensitivity $m$). Consequently, the CPU time needed to solve these equations is generally very important compared to the case of a rate-independent formulation. Plastic deformation develops mainly through three successive stages: (i) a homogeneous deformation; (ii) a progressively concentrating strain under a constant or smoothly decreasing load (diffuse necking), and (iii) an abrupt strain localization (localized necking) under a rapid load decrease. The incipience of localized necking represents the ultimate deformation that a stretched metal sheet can undergo, since this phenomenon is often precursor to material failure. To predict the onset of diffuse necking, several criteria have been developed in the literature. In the context of diffuse necking criteria, one can quote the maximum force criterion initially proposed by Considère (1885). This criterion, applicable in its original form in the case of uniaxial tension loading, assumes that diffuse necking is reached when the tension force reaches its maximum value. This condition is equivalent to the equality between the stress $\sigma$ and the strain-hardening rate $d\sigma/d\varepsilon$. Subsequently, Swift (1952) extended the Considère criterion to biaxial loadings. In the present study, focus is restricted to the prediction of macroscopic localized necking using the Rice bifurcation theory (Rice, 1976). This bifurcation corresponds mathematically to the singularity of the macroscopic acoustic tensor. The macroscopic tangent modulus is numerically evaluated using the condensation technique (Zhu et al., 2022) in order to determine the acoustic tensor. Compared to the initial imperfection approach (Marciniak and Kuczyński, 1967) commonly used in previous contributions based on multiscale schemes, the Rice bifurcation approach presents at least two conceptual and practical benefits. In fact, in addition to its sound theoretical foundation, the bifurcation approach does not require any fitting parameter, such as the initial imperfection size needed in the initial imperfection approach. Furthermore, the CPU time required to predict an FLD by the bifurcation theory is significantly lower than its counterpart in the case of the initial imperfection analysis (Akpama et al., 2017). The application of the Rice bifurcation approach in conjunction with the CPFEM allows constructing realistic forming limit diagrams. The main reason of these observations is the presence of typical destabilizing effects, as a natural outcome of crystal plasticity, through the formation of vertices at the current points of the Schmid yield locus. Bifurcation and thus the corresponding ductility limits cannot be reached if a rate-dependent formulation is used to model the single crystal constitutive framework. It should be noted that, in the literature, several other destabilizing mechanisms have been incorporated in various constitutive frameworks to predict the ductility limits by the Rice bifurcation criterion. These destabilizing phenomena are generally due to the application of the deformation theory of plasticity, as in Ben Bettaieb and Abed-Meraim (2015), or the use of a non-associative flow rule (Ben Bettaieb and Abed-Meraim, 2021; Jedidi et al., 2020). Destabilizing phenomena may also be induced by softening behavior incorporated in the constitutive modeling through coupling with damage (see, e.g., Haddag et al. (2009), within the framework of CDM, and Mansouri et al., 2014, for micromechanics-based constitutive models).

Particular attention is focused on the study of the effect of both morphological and crystallographic textures on the onset of plastic strain localization. In this aim, the NEPER software (Quey et al., 2011), based on the Voronoi tessellation technique, is used to generate unit cells with three different grain morphologies (namely, cube, random and elongated morphology). Note that the use of the Voronoi technique offers interesting possibilities, as realistic grain morphologies can be accurately described unlike mean-field schemes, which are very limited in this regard. In this technique, each grain is made up of several finite elements and each finite element contains several integration points. Hence, the proposed numerical strategy (based on the FEM approach) allows taking into account the effect of the heterogeneity of mechanical fields within the grains, thus leading to a better description of experimental evidences (Kanjarla et al., 2010). To investigate the effect of crystallographic texture, we have used the ATEX software (Beausir and Fundenberger, 2017) to generate three crystallographic textures: random, cube and copper texture. Numerical predictions obtained in this work reveal that the effect of both morphological and crystallographic textures is more noticeable for positive strain paths. This result is consistent with several contributions in the literature (see for instance, Barlat, 1987; Akpama et al., 2017). Furthermore, the numerical trends clearly show that the effect of crystallographic texture on the predicted limit strains is more important than that of morphological texture.

The remainder of the paper is organized as follows:

- Section 2 provides some details about the design of the CPFEM-based strategy. The main lines of the periodic homogenization method, the crystal plasticity finite element method and the Rice bifurcation approach are briefly reviewed.
- The numerical results obtained using the developed FEM approach are presented and extensively discussed in Section 3.
- A summary of the results and conclusions is provided in Section 4.

## 2. Methodology and theory

### 2.1. Design of the CPFEM-based multiscale strategy

The main goal of this study is to use a CPFEM-based multiscale scheme to evaluate the effect of various morphological and crystallographic textures on the ductility limits of face-centered cubic (FCC) polycrystalline aggregates. Fig. 1 summarizes the schematic representation of this multiscale strategy. Unless explicitly stated otherwise, the aggregates used in the following simulations are represented by a unit cell of cubic initial shape and of initial volume $\mathcal{V}_0$ equal to $l_0^3$. The morphology of the grains constituting these aggregates are generated, on the basis of the Voronoi tessellation technique, using the free (open-source) software package NEPER (Quey et al., 2011). The generated unit cells are then discretized into finite element meshes using the Gmsh package of NEPER software, where 20-node quadratic hexahedral finite elements with full integration (27 integration points

by element) are used (element C3D20 in ABAQUS). Hence, each grain is composed of several finite elements. Each individual integration point of the finite elements represents a single crystal. All the single crystals belonging the same grain have the same initial crystallographic orientation. The initial crystallographic textures are generated by the ATEX software (Beausir and Fundenberger, 2017). A Python script is developed to assign these initial orientations to the different integration points. During loading, the deformation of the different single crystals belonging to a grain may evolve differently, thus leading to heterogeneity of the mechanical fields inside the same grain (crystallographic orientation, plastic deformation, stress...). The resulting file obtained from the NEPER software (an ABAQUS input file) is then transferred to ABAQUS to apply the periodic boundary conditions and the macroscopic loading on the aggregates. To perform this task, the set of Python scripts called HOMTOOLS and developed by Lejeunes and Bourgeois (2011) is used. Further details about the use of the HOMTOOLS will be given in Section 2.2. The single crystal constitutive equations solved at each integration point follow a rate-independent formulation, where the flow rule is modeled by the Schmid law. These constitutive equations are implemented via a user-defined material subroutine UMAT into ABAQUS/Standard finite element code. A brief description of these constitutive equations and the corresponding algorithm used to integrate them will be provided in Section 2.4 and Appendix B, respectively. The ductility limits of the polycrystalline aggregates are predicted by the Rice bifurcation theory. This theory states that bifurcation takes place when the macroscopic acoustic tensor becomes singular. This acoustic tensor is built from the macroscopic elastoplastic tangent modulus which is obtained by condensation of the global stiffness matrix. To perform the bifurcation analysis, we have developed a set of Python codes allowing us to achieve the following elementary tasks: assembly of the elementary stiffness matrices into the corresponding global one, condensation of the global stiffness matrix to compute the macroscopic tangent operator and then to check the singularity of the acoustic tensor. The elementary stiffness matrices are obtained from the finite element simulations using the output option 'Element Matrix Output', which needs to be added in the ABAQUS input file. These elementary matrices are stored in a file having the extension '.mtx'. More technical and practical details about the application of the bifurcation analysis in connection with ABAQUS are provided in Zhu et al. (2022). A brief presentation of the theoretical and numerical aspects related to the Rice bifurcation theory is given in Section 2.5.

### 2.2. Macroscopic boundary conditions

The polycrystalline aggregates (called also unit cells using the periodic homogenization terminology) are subjected to periodic boundary conditions (PBCs) to predict ductility limits in the current investigation. The ABAQUS plug-ins HOMTOOLS developed by Lejeunes and Bourgeois (2011) are used to automatically apply these PBCs. To be consistent with classical FLD predictions, a macroscopic plane stress state in the direction normal to the sheet plane is assumed ($Z$ direction, as shown in Fig. 4(d)). Then, the PBCs are applied on the faces $S_{01}^{-} : x_{01} = -\frac{l_0}{2}; S_{01}^{+} : x_{01} = \frac{l_0}{2}, S_{02}^{-} : x_{02} = -\frac{l_0}{2}; S_{02}^{+} : x_{02} = \frac{l_0}{2}$, while faces $S_{03}^{-} : x_{03} = -\frac{l_0}{2}; S_{03}^{+} : x_{03} = \frac{l_0}{2}$ are kept stress free (see Fig. 4(d)). To formulate the periodic homogenization equations and then to apply the macroscopic loading on the unit cells, the deformation gradient $\mathbf{F}$ and the first Piola–Kirchhoff stress tensor $\mathbf{P}$ are adopted as appropriate work-conjugate deformation and stress measures. The main lines of the periodic homogenization equations will be given in Section 2.3. Under the in-plane biaxial stretching conditions required in the prediction of unit cell FLDs, the macroscopic tensors $\mathbf{F}$ and $\mathbf{P}$ should have the following generic forms:

$$\mathbf{F} = \begin{pmatrix} F_{11} & 0 & * \\ 0 & F_{22} & * \\ * & * & * \end{pmatrix}; \quad \mathbf{P} = \begin{pmatrix} * & * & 0 \\ * & * & 0 \\ 0 & 0 & 0 \end{pmatrix}, \tag{1}$$

where the components denoted by '*' are unknown and need to be determined by finite element computations. Furthermore, the unit cell is subjected to proportional strain paths, defined by constant strain ratio $\rho$:

$$\rho = \frac{E_{22}}{E_{11}} = \frac{Ln(F_{22})}{Ln(F_{11})} = constant, \tag{2}$$

where $E_{11}$ and $E_{22}$ are the components of the macroscopic logarithmic strain tensor $\mathbf{E}$, and $\rho$ ranges between $-0.5$ and 1 to span the complete FLD.

### 2.3. Periodic homogenization method

The periodic homogenization technique is used to determine the macroscopic mechanical behavior of the unit cell from that of the individual grains and to apply the boundary conditions detailed in Section 2.2. For the sake of brevity, only the main lines of this multiscale scheme are provided in the following subsections (Section 2.3.1 for the theoretical formulation and Section 2.3.2 for the numerical treatment). The readers interested in additional details about this multiscale scheme can refer to Ben Bettaieb et al. (2012), Zhu et al. (2020a,b) and Zhu et al. (2022).

#### 2.3.1. Periodic homogenization equations

The periodic homogenization technique is defined by the following equations and properties:

- The macroscopic deformation gradient $\mathbf{F}$ and the first Piola–Kirchhoff stress tensor $\mathbf{P}$ are connected to their microscopic counterparts $\mathbf{f}$ and $\mathbf{p}$ by the following averaging relations (over the initial volume $\mathcal{V}_0$ of the unit cell):

$$\mathbf{F} = \frac{1}{|\mathcal{V}_0|}\int_{\mathcal{V}_0} \mathbf{f} d\mathcal{V}_0; \quad \mathbf{P} = \frac{1}{|\mathcal{V}_0|}\int_{\mathcal{V}_0} \mathbf{p} d\mathcal{V}_0. \tag{3}$$

The rate form of the averaging relations Eq. (3), more suitable to numerical formulation, can be derived as follows:

$$\dot{\mathbf{F}} = \frac{1}{|\mathcal{V}_0|}\int_{\mathcal{V}_0} \dot{\mathbf{f}} d\mathcal{V}_0; \quad \dot{\mathbf{P}} = \frac{1}{|\mathcal{V}_0|}\int_{\mathcal{V}_0} \dot{\mathbf{p}} d\mathcal{V}_0. \tag{4}$$

- The periodicity conditions of the microscopic variables state that the in-plane microscopic deformation gradient ${}^{\mathrm{IN}}\mathbf{f}$ and the in-plane first Piola–Kirchhoff stress tensor ${}^{\mathrm{IN}}\mathbf{p}$ are periodic over the side set $S_0 = S_{01}^{-} \cup S_{01}^{+} \cup S_{02}^{-} \cup S_{02}^{+}$. The periodicity of ${}^{\mathrm{IN}}\mathbf{f}$ implies that its rate ${}^{\mathrm{IN}}\dot{\mathbf{f}}$ can be split into its macroscopic counterpart ${}^{\mathrm{IN}}\dot{\mathbf{F}}$ and a superimposed fluctuation gradient ${}^{\mathrm{IN}}\dot{\mathbf{f}}_{per}$ that is periodic over $S_0$:

$${}^{\mathrm{IN}}\dot{\mathbf{f}} = {}^{\mathrm{IN}}\dot{\mathbf{F}} + {}^{\mathrm{IN}}\dot{\mathbf{f}}_{per}; \text{ where } {}^{\mathrm{IN}}\dot{\mathbf{f}} = \begin{pmatrix} \dot{f}_{11} & \dot{f}_{12} \\ \dot{f}_{21} & \dot{f}_{22} \end{pmatrix} \text{ and } {}^{\mathrm{IN}}\dot{\mathbf{F}} = \begin{pmatrix} \dot{F}_{11} & \dot{F}_{12} \\ \dot{F}_{21} & \dot{F}_{22} \end{pmatrix}. \tag{5}$$

Spatial integration of Eq. (5) enables to obtain the in-plane velocity ${}^{\mathrm{IN}}\dot{\mathbf{u}}$ of a material point:

$${}^{\mathrm{IN}}\dot{\mathbf{u}} = {}^{\mathrm{IN}}\dot{\mathbf{F}} \cdot {}^{\mathrm{IN}}\mathbf{x}_0 + {}^{\mathrm{IN}}\dot{\mathbf{u}}_{per}, \tag{6}$$

where ${}^{\mathrm{IN}}\mathbf{x}_0$ represents the initial in-plane coordinates of the material point, and ${}^{\mathrm{IN}}\dot{\mathbf{u}}_{per}$ is an in-plane periodic velocity field.

- The microscopic static equilibrium equation is defined by the following rate form (when body forces are neglected):

$$div_{\mathbf{x}_0}(\dot{\mathbf{p}}) = \mathbf{0}. \tag{7}$$

- The microscopic constitutive equations are formulated at the single crystal scale and will be summarized in Section 2.4.

#### 2.3.2. Numerical implementation

The aforementioned periodic homogenization problem defined on the unit cell is solved by the finite element method. As a departure

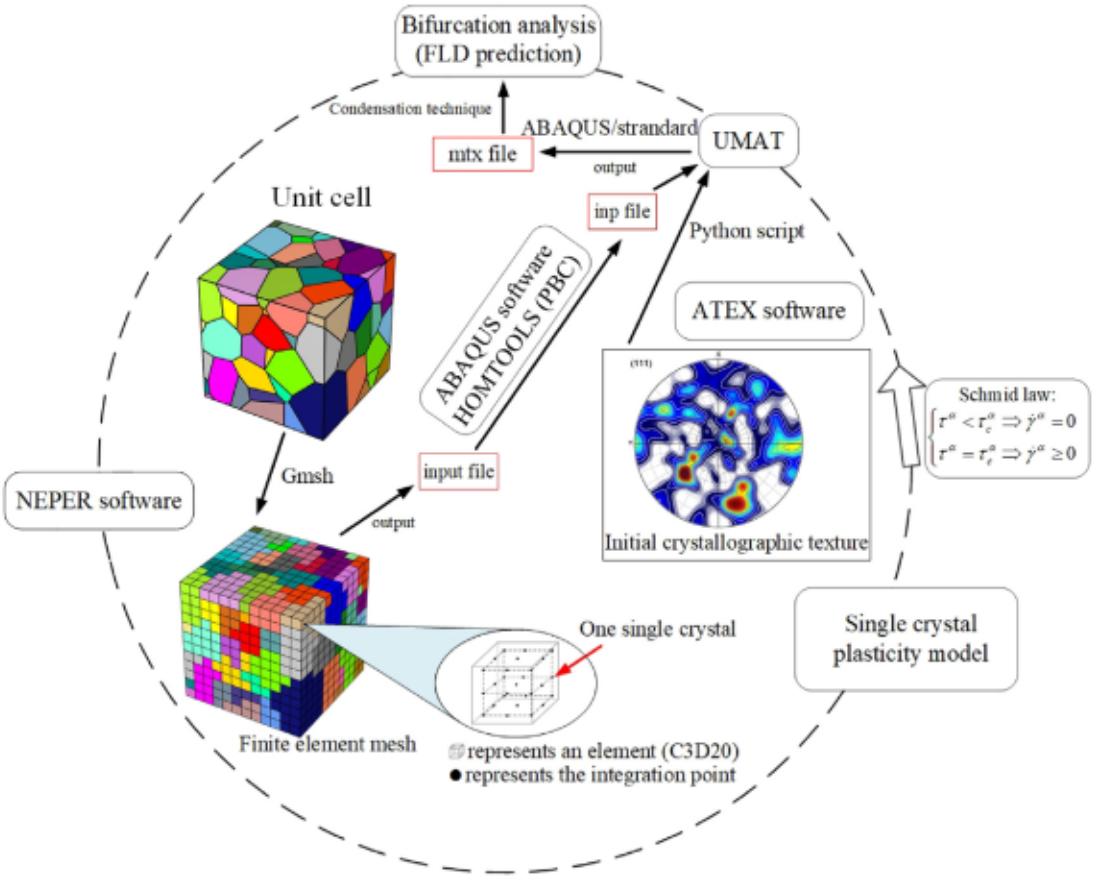


**Fig. 1.** Schematic presentation of the CPFEM-based multiscale scheme used in the ductility limit predictions.

point of the numerical treatment of this problem, the virtual power principle should be formulated for an arbitrary virtual velocity $\delta\dot{\mathbf{u}}$ (using the microscopic equilibrium Eq. (7)):

$$div_{\mathbf{x}_0}(\dot{\mathbf{p}}) \cdot \delta\dot{\mathbf{u}} = 0. \tag{8}$$

Then, integrating Eq. (8) over the initial volume $\mathcal{V}_0$ of the unit cell yields:

$$\int_{\mathcal{V}_0} div_{\mathbf{x}_0}(\dot{\mathbf{p}}) \cdot \delta\dot{\mathbf{u}} d\mathcal{V}_0 = 0. \tag{9}$$

Using the chain rule and the divergence theorem, Eq. (9) can be rewritten as:

$$\int_{\mathcal{V}_0} \left[\frac{\partial\delta\dot{\mathbf{u}}}{\partial\mathbf{x}_0} : \dot{\mathbf{p}}\right] d\mathcal{V}_0 = \int_{S_0\cup S_{03}^-\cup S_{03}^+} \delta\dot{\mathbf{u}} \cdot \dot{\mathbf{p}} \cdot \vec{\mathbf{n}}_0 dS_0. \tag{10}$$

The plane stress assumption implies that vector $\dot{\mathbf{p}} \cdot \vec{\mathbf{n}}_0$ vanishes over the set of faces $S_{03}^- \cup S_{03}^+$. Then, the right-hand side of Eq. (10) can be recast as:

$$\begin{aligned}\int_{S_0\cup S_{03}^-\cup S_{03}^+} \delta\dot{\mathbf{u}} \cdot \dot{\mathbf{p}} \cdot \vec{\mathbf{n}}_0 dS_0 &= \int_{S_0} \delta\dot{\mathbf{u}} \cdot \dot{\mathbf{p}} \cdot \vec{\mathbf{n}}_0 dS_0 + \int_{S_{03}^-\cup S_{03}^+} \delta\dot{\mathbf{u}} \cdot \dot{\mathbf{p}} \cdot \vec{\mathbf{n}}_0 dS_0;\\ &= \int_{S_0} \delta\dot{\mathbf{u}} \cdot \dot{\mathbf{p}} \cdot \vec{\mathbf{n}}_0 dS_0;\\ &= \int_{S_0} \delta^{\mathrm{IN}}\dot{\mathbf{u}} \cdot {}^{\mathrm{IN}}\dot{\mathbf{p}} \cdot {}^{\mathrm{IN}}\vec{\mathbf{n}}_0 dS_0. \end{aligned} \tag{11}$$

Hence, the left-hand side of Eq. (10) can be rewritten as:

$$\begin{aligned}\int_{\mathcal{V}_0} \left[\frac{\partial\delta\dot{\mathbf{u}}}{\partial\mathbf{x}_0} : \dot{\mathbf{p}}\right] d\mathcal{V}_0 &= \int_{S_0} \delta^{\mathrm{IN}}\dot{\mathbf{u}} \cdot {}^{\mathrm{IN}}\dot{\mathbf{p}} \cdot {}^{\mathrm{IN}}\vec{\mathbf{n}}_0 dS_0;\\ &= \int_{\mathcal{V}_0} \left[\left(\delta^{\mathrm{IN}}\dot{\mathbf{F}} + \frac{\partial\delta^{\mathrm{IN}}\dot{\mathbf{u}}_{per}}{\partial^{\mathrm{IN}}\mathbf{x}_0}\right) : {}^{\mathrm{IN}}\dot{\mathbf{p}}\right] d\mathcal{V}_0;\\ &= \int_{\mathcal{V}_0} \left[\delta^{\mathrm{IN}}\dot{\mathbf{F}} : {}^{\mathrm{IN}}\dot{\mathbf{p}}\right] d\mathcal{V}_0 + \int_{\mathcal{V}_0} \left[\frac{\partial\delta^{\mathrm{IN}}\dot{\mathbf{u}}_{per}}{\partial^{\mathrm{IN}}\mathbf{x}_0} : {}^{\mathrm{IN}}\dot{\mathbf{p}}\right] d\mathcal{V}_0;\\ &= |\mathcal{V}_0|\delta^{\mathrm{IN}}\dot{\mathbf{F}} : {}^{\mathrm{IN}}\dot{\mathbf{P}} + \int_{S_0} \left[\left(\delta^{\mathrm{IN}}\dot{\mathbf{u}}_{per} \otimes {}^{\mathrm{IN}}\vec{\mathbf{n}}_0\right) : {}^{\mathrm{IN}}\dot{\mathbf{p}}\right] dS_0. \end{aligned} \tag{12}$$

Considering the anti-periodicity of tensor $\delta^{\mathrm{IN}}\dot{\mathbf{u}}_{per} \otimes {}^{\mathrm{IN}}\vec{\mathbf{n}}_0$ and the periodicity of ${}^{\mathrm{IN}}\dot{\mathbf{p}}$ (as the first Piola–Kirchhoff stress tensor $\mathbf{p}$ is periodic), we can easily demonstrate that:

$$\int_{S_0} \left[\left(\delta^{\mathrm{IN}}\dot{\mathbf{u}}_{per} \otimes {}^{\mathrm{IN}}\vec{\mathbf{n}}_0\right) : {}^{\mathrm{IN}}\dot{\mathbf{p}}\right] dS_0 = 0. \tag{13}$$

The combination of Eqs. (12) and (13), leads to the Lagrangian formulation of the Hill–Mandel lemma, which remains valid under the plane stress assumption:

$$\int_{\mathcal{V}_0} \left[\frac{\partial\delta\dot{\mathbf{u}}}{\partial\mathbf{x}_0} : \dot{\mathbf{p}}\right] d\mathcal{V}_0 = |\mathcal{V}_0|\delta^{\mathrm{IN}}\dot{\mathbf{F}} : {}^{\mathrm{IN}}\dot{\mathbf{P}}. \tag{14}$$

To numerically enforce Eq. (14) and hence to apply the macroscopic loading as well as the PBCs, the macroscopic reference point technique is used. This technique is automatically managed using the set of Python codes HOMTOOLS developed in Lejeunes and Bourgeois (2011). Practical details about the application of this technique to predict localized necking under biaxial loading are provided in Zhu et al. (2020a) and Zhu et al. (2020b).

### 2.4. Single crystal plasticity model

The single crystal behavior is assumed to be elasto-plastic and follows a rate-independent theory. In this framework, the microscopic deformation gradient $\mathbf{f}$, determined at each integration point by finite element computation, can be multiplicatively decomposed into an

$$\bar{\mathbf{r}} = \begin{bmatrix} cos\varphi_1 cos\varphi_2 - sin\varphi_1 sin\varphi_2 cos\phi & sin\varphi_1 cos\varphi_2 + cos\varphi_1 sin\varphi_2 cos\phi & sin\varphi_2 sin\phi \\ -cos\varphi_1 sin\varphi_2 - sin\varphi_1 cos\varphi_2 cos\phi & -sin\varphi_1 sin\varphi_2 + cos\varphi_1 cos\varphi_2 cos\phi & cos\varphi_2 sin\phi \\ sin\varphi_1 sin\phi & -cos\varphi_1 sin\phi & cos\phi \end{bmatrix}. \tag{17}$$

**Box I.**

elastic part $\mathbf{f}^e$ and a plastic part $\mathbf{f}^p$, as follows:

$$\mathbf{f} = \mathbf{f}^e \cdot \mathbf{f}^p, \tag{15}$$

where the elastic part $\mathbf{f}^e$ is obtained from a stretching tensor $\mathbf{v}^e$ and a rotation tensor $\bar{\mathbf{r}}$ through the following multiplicative decomposition:

$$\mathbf{f}^e = \mathbf{v}^e \cdot \bar{\mathbf{r}}. \tag{16}$$

The rotation tensor $\bar{\mathbf{r}}$ defines the orientation of the crystallographic lattice with respect to the current microscopic coordinate system. This rotation is parameterized by the Euler angles $\varphi_1$, $\phi$, and $\varphi_2$ (based on the Bunge convention) as shown by the matrix formulation as Eq. (17) that is given in Box I.

The microscopic velocity gradient $\mathbf{g}$, more suitable as deformation measure in the formulation of the single crystal constitutive framework, can be determined from the total deformation gradient $\mathbf{f}$ as:

$$\begin{aligned} \mathbf{g} &= \dot{\mathbf{f}} \cdot \mathbf{f}^{-1} = \dot{\mathbf{f}}^e \cdot \mathbf{f}^{e-1} + \mathbf{f}^e \cdot \dot{\mathbf{f}}^p \cdot \mathbf{f}^{p-1} \cdot \mathbf{f}^{e-1}; \\ &= \dot{\mathbf{v}}^e \cdot \mathbf{v}^{e-1} + \mathbf{v}^e \cdot \dot{\bar{\mathbf{r}}} \cdot \bar{\mathbf{r}}^T \cdot \mathbf{v}^{e-1} + \mathbf{v}^e \cdot \bar{\mathbf{r}} \cdot \dot{\mathbf{f}}^p \cdot \mathbf{f}^{p-1} \cdot \bar{\mathbf{r}}^T \cdot \mathbf{v}^{e-1}. \end{aligned} \tag{18}$$

As is the case for most metallic materials, the elastic deformation is often assumed to be very small compared to unity. Accordingly, the stretching tensor $\mathbf{v}^e$ is very close to the second-order identity tensor:

$$\mathbf{v}^e \approx \mathbf{1}. \tag{19}$$

Combining Eqs. (18) and (19), we obtain:

$$\mathbf{g} = \dot{\mathbf{v}}^e + \dot{\bar{\mathbf{r}}} \cdot \bar{\mathbf{r}}^T + \bar{\mathbf{r}} \cdot \dot{\mathbf{f}}^p \cdot \mathbf{f}^{p-1} \cdot \bar{\mathbf{r}}^T. \tag{20}$$

The velocity gradient $\mathbf{g}$ can be additively decomposed into its symmetric and skew-symmetric parts, denoted as $\mathbf{d}$ and $\mathbf{w}$, respectively:

$$\mathbf{g} = \mathbf{d} + \mathbf{w}, \tag{21}$$

where the symmetric (respectively skew-symmetric) part can also be decomposed into an elastic part $\mathbf{d}^e$ (respectively $\mathbf{w}^e$) and a plastic part $\mathbf{d}^p$ (respectively $\mathbf{w}^p$):

$$\mathbf{d} = \frac{1}{2}(\mathbf{g} + \mathbf{g}^T) = \mathbf{d}^e + \mathbf{d}^p; \quad \mathbf{w} = \frac{1}{2}(\mathbf{g} - \mathbf{g}^T) = \mathbf{w}^e + \mathbf{w}^p, \tag{22}$$

with

$$\mathbf{d}^e = \dot{\mathbf{v}}^e; \quad \mathbf{d}^p = \bar{\mathbf{r}} \cdot (\dot{\mathbf{f}}^p \cdot \mathbf{f}^{p-1})_{sym} \cdot \bar{\mathbf{r}}^T; \quad \mathbf{w}^e = \dot{\bar{\mathbf{r}}} \cdot \bar{\mathbf{r}}^T; \quad \mathbf{w}^p = \bar{\mathbf{r}} \cdot (\dot{\mathbf{f}}^p \cdot \mathbf{f}^{p-1})_{skew-sym} \cdot \bar{\mathbf{r}}^T. \tag{23}$$

Because the plastic deformation is caused by the slip on the crystallographic systems, the plastic part of the velocity gradient $\mathbf{g}$ can be expressed as:

$$\mathbf{d}^p + \mathbf{w}^p = \sum_{\alpha=1}^{N_s} \dot{\gamma}^\alpha (\vec{\mathbf{m}}^\alpha \otimes \vec{\mathbf{n}}^\alpha), \tag{24}$$

where:

- $N_s$ is the total number of slip systems, equal to 12 for FCC single crystals.
- $\dot{\gamma}^\alpha$ is the algebraic value of the slip rate of slip system $\alpha$.
- $\vec{\mathbf{m}}^\alpha$ is the slip direction vector, while $\vec{\mathbf{n}}^\alpha$ is the vector normal to the slip plane.

For practical reasons and to handle only positive values of slip rates, it is more convenient to decompose each slip system into two opposite oriented slip systems $(\vec{\mathbf{m}}^\alpha, \vec{\mathbf{n}}^\alpha)$ and $(-\vec{\mathbf{m}}^\alpha, \vec{\mathbf{n}}^\alpha)$. The plastic strain rate $\mathbf{d}^p$ and plastic spin $\mathbf{w}^p$ can be rewritten in terms of the symmetric and skew-symmetric parts of the Schmid tensor as follows:

$$\mathbf{d}^p = \sum_{\alpha=1}^{2N_s} \dot{\gamma}^\alpha \mathbf{R}^\alpha; \quad \mathbf{w}^p = \sum_{\alpha=1}^{2N_s} \dot{\gamma}^\alpha \mathbf{S}^\alpha, \tag{25}$$

where $\mathbf{R}^\alpha$ and $\mathbf{S}^\alpha$ are defined as:

$$\mathbf{R}^\alpha = \left(\vec{\mathbf{m}}^\alpha \otimes \vec{\mathbf{n}}^\alpha\right)_{sym}; \quad \mathbf{S}^\alpha = \left(\vec{\mathbf{m}}^\alpha \otimes \vec{\mathbf{n}}^\alpha\right)_{skew-sym}. \tag{26}$$

The rotation $\bar{\mathbf{r}}$ is chosen to transform the Schmid tensor $\vec{\mathbf{m}}^\alpha \otimes \vec{\mathbf{n}}^\alpha$ of each slip system $\alpha$ so that it remains constant when expressed in the intermediate configuration and equal to $\vec{\mathbf{m}}_0^\alpha \otimes \vec{\mathbf{n}}_0^\alpha$ (see Fig. 2):

$$\vec{\mathbf{m}}_0^\alpha \otimes \vec{\mathbf{n}}_0^\alpha = \bar{\mathbf{r}}^T \cdot \left(\vec{\mathbf{m}}^\alpha \otimes \vec{\mathbf{n}}^\alpha\right) \cdot \bar{\mathbf{r}}. \tag{27}$$

The detailed information on the slip systems for FCC single crystals is given in Appendix A.

To satisfy the objectivity principle, Eqs. (22) and (25) can be rewritten in the crystal lattice frame defined by rotation $\bar{\mathbf{r}}$. For the sake of clarity, tensors and vectors evaluated in this frame are denoted by an over-line notation. In this frame, the velocity gradient $\bar{\mathbf{g}}$ is expressed as follows:

$$\begin{aligned} \bar{\mathbf{g}} &= \bar{\mathbf{r}}^T \cdot \mathbf{g} \cdot \bar{\mathbf{r}} = \bar{\mathbf{d}} + \bar{\mathbf{w}}; \\ &= \bar{\mathbf{d}}^e + \bar{\mathbf{d}}^p + \bar{\mathbf{w}}^e + \bar{\mathbf{w}}^p, \end{aligned} \tag{28}$$

and the plastic parts $\bar{\mathbf{d}}^p$ and $\bar{\mathbf{w}}^p$ can be expressed as:

$$\bar{\mathbf{d}}^p = \sum_{\alpha=1}^{2N_s} \dot{\gamma}^\alpha \mathbf{R}_0^\alpha; \quad \bar{\mathbf{w}} = \sum_{\alpha=1}^{2N_s} \dot{\gamma}^\alpha \mathbf{S}_0^\alpha; \quad \text{with} \quad \dot{\gamma}^\alpha \geq 0, \tag{29}$$

where $\mathbf{R}_0^\alpha$ and $\mathbf{S}_0^\alpha$ are expressed in the intermediate configuration as:

$$\mathbf{R}_0^\alpha = \left(\vec{\mathbf{m}}_0^\alpha \otimes \vec{\mathbf{n}}_0^\alpha\right)_{sym}; \quad \mathbf{S}_0^\alpha = \left(\vec{\mathbf{m}}_0^\alpha \otimes \vec{\mathbf{n}}_0^\alpha\right)_{skew-sym}. \tag{30}$$

The elastic behavior is assumed to be linear isotropic and, given by the Hooke law:

$$\hat{\boldsymbol{\sigma}} = \bar{\mathbf{c}}^e : \left(\bar{\mathbf{d}} - \bar{\mathbf{d}}^p\right), \tag{31}$$

where $\bar{\mathbf{c}}^e$ is the fourth-order elastic stiffness tensor, which depends on the Young modulus $E$ and the Poisson ratio $\nu$.

The plastic flow rule is defined by the Schmid law, which indicates that slip may occur only when the resolved shear stress $\tau^\alpha$ on a slip system $\alpha$ becomes equal to a critical value $\tau_c^\alpha$:

$$\forall \alpha = 1, \ldots, 2N_s : \begin{cases} \tau^\alpha < \tau_c^\alpha & \Rightarrow \dot{\gamma}^\alpha = 0 \\ \tau^\alpha = \tau_c^\alpha & \Rightarrow \dot{\gamma}^\alpha \geq 0, \end{cases} \tag{32}$$

where the resolved shear stress $\tau^\alpha$ is defined in term of the Cauchy stress tensor $\boldsymbol{\sigma}$ and the symmetric part of the Schmid tensor $\vec{\mathbf{m}}^\alpha \otimes \vec{\mathbf{n}}^\alpha$:

$$\forall \alpha = 1, \ldots, 2N_s : \tau^\alpha = \boldsymbol{\sigma} : \mathbf{R}^\alpha = \bar{\boldsymbol{\sigma}} : \mathbf{R}_0^\alpha. \tag{33}$$

The critical shear stress $\tau_c^\alpha$ is often expressed in a rate form to make it suitable to numerical implementation as:

$$\forall \alpha = 1, \ldots, N_s : \dot{\tau}_c^\alpha = \dot{\tau}_c^{\alpha+N_s} = \sum_{\beta=1}^{N_s} H^{\alpha\beta} \left(\dot{\gamma}^\beta + \dot{\gamma}^{\beta+N_s}\right). \tag{34}$$

The initial value of the critical shear stress $\tau_{c0}$ (the same for all the crystallographic slip systems) is assumed to depend on the grain size

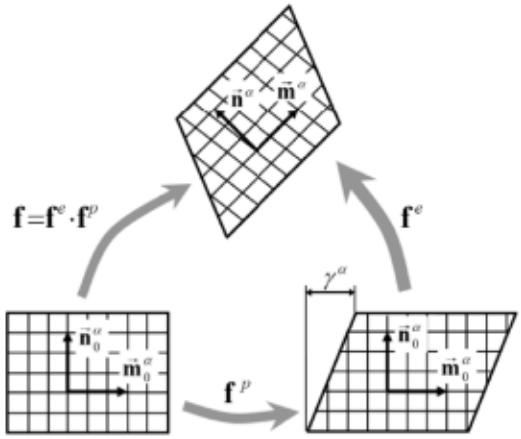


**Fig. 2.** Schematic representation of the multiplicative decomposition of the deformation gradient: plastic slip and rigid rotation along with elastic distortion of the crystallographic lattice.

as follows:

$$\tau_{c0} = \tau_0 + \frac{\kappa_{HP}}{\sqrt{d_{eff}}}, \tag{35}$$

where $\tau_0$ is the initial critical shear stress, $\kappa_{HP}$ is the microscopic Hall–Petch constant and $d_{eff}$ is the average of the equivalent grain diameters (i.e., diameter of the sphere of equivalent volume). The Hall–Petch effect will be considered in detail only in Section 3.5.1. In the other sections, the grain size effect is not considered, allowing us to confine attention to other effects, such as crystallographic and morphological texture, and sheet thickness.

The adopted hardening behavior is described by an isotropic non-linear model of power type, given by the following equation (Yoshida and Kuroda, 2012; Signorelli et al., 2021):

$$\forall \alpha, \beta = 1, \dots, N_s \,:\, H^{\alpha\beta} = h_0 \left(1 + \frac{h_0 \Gamma}{\tau_{c0}\, n}\right)^{n-1}, \tag{36}$$

where $h_0$ and $n$ are hardening parameters. As to $\Gamma$, it represents the accumulated slip given by:

$$\Gamma = \sum_{\alpha=1}^{2N_s} \gamma^\alpha. \tag{37}$$

The constitutive equations are implemented within ABAQUS/Standard finite element code via a user-defined material subroutine UMAT. An explicit ultimate algorithm is adopted to integrate these constitutive equations, which has been shown to be more efficient and robust than other integration algorithms (Akpama et al., 2016). The main steps of this integration algorithm are presented in Appendix B.

### 2.5. Rice bifurcation criterion

The Rice bifurcation criterion, initially proposed in Rudnicki and Rice (1975) and Rice (1976), is used to determine the occurrence of localized necking. This criterion is associated with a jump in the strain rate across a localization band, as shown in Fig. 3, and it can be mathematically interpreted by the loss of ellipticity of the governing macroscopic equilibrium equations. This criterion can be derived from the following two conditions:

- The first condition: the kinematic condition for the strain rate jump, which can be described as follows:

$$[[{}^{\mathrm{IN}}\dot{\mathbf{F}}]] = {}^{\mathrm{IN}}\dot{\mathbf{F}}^{\mathrm{O}} - {}^{\mathrm{IN}}\dot{\mathbf{F}}^{\mathrm{I}} = \dot{\vec{C}} \otimes \vec{\mathcal{N}}, \tag{38}$$

where:

- $[[{}^{\mathrm{IN}}\dot{\mathbf{F}}]]$ is the jump of the velocity gradient field ${}^{\mathrm{IN}}\dot{\mathbf{F}}$ across the localization band. ${}^{\mathrm{IN}}\dot{\mathbf{F}}^{\mathrm{O}}$ and ${}^{\mathrm{IN}}\dot{\mathbf{F}}^{\mathrm{I}}$ are the velocity gradient outside and inside the band, respectively.
- $\dot{\vec{C}}$ is the jump vector.
- $\vec{\mathcal{N}}$ is the unit vector normal to the localization band, equal to $(cos\theta, sin\theta)$, where $0 \le \theta \le \pi/2$.

- The second condition: the force equilibrium condition across the band should be satisfied. This condition can be expressed in terms of the rate of in-plane macroscopic first Piola–Kirchhoff stress tensor ${}^{\mathrm{IN}}\dot{\mathbf{P}}$:

$$[[{}^{\mathrm{IN}}\dot{\mathbf{P}}]] \cdot \vec{\mathcal{N}} = \vec{\mathbf{0}}. \tag{39}$$

On the other hand, the constitutive law at the macroscopic scale, which relates the in-plane macroscopic tensors ${}^{\mathrm{IN}}\dot{\mathbf{F}}$ and ${}^{\mathrm{IN}}\dot{\mathbf{P}}$ via the in-plane macroscopic tangent modulus ${}^{\mathrm{IN}}\mathbf{B}$, is expressed as:

$${}^{\mathrm{IN}}\dot{\mathbf{P}} = {}^{\mathrm{IN}}\mathbf{B} \,:\, {}^{\mathrm{IN}}\dot{\mathbf{F}}. \tag{40}$$

Combining these two conditions (Eqs. (38) and (39)) with the constitutive law Eq. (40) yields:

$$\left[{}^{\mathrm{IN}}\mathbf{B} \,:\, \left(\dot{\vec{C}} \otimes \vec{\mathcal{N}}\right)\right] \cdot \vec{\mathcal{N}} = \vec{\mathbf{0}}, \tag{41}$$

which is equivalent to:

$$\left(\vec{\mathcal{N}} \cdot {}^{\mathrm{IN}}\mathbf{C} \cdot \vec{\mathcal{N}}\right) \cdot \dot{\vec{C}} = \vec{\mathbf{0}}, \tag{42}$$

where ${}^{\mathrm{IN}}\mathbf{C}$ is the fourth-order tensor obtained from the in-plane macroscopic tangent modulus ${}^{\mathrm{IN}}\mathbf{B}$ by permutation of the first two indices (${}^{\mathrm{IN}}C_{ijkl} = {}^{\mathrm{IN}}B_{jikl}$ for $\forall i, j, k, l \;:\; 1, 2, 3$). Tensor $\vec{\mathcal{N}} \cdot {}^{\mathrm{IN}}\mathbf{C} \cdot \vec{\mathcal{N}}$ is the so-called acoustic tensor. Strain localization occurs when the acoustic tensor becomes singular and the corresponding determinant vanishes.

$$\det\left(\vec{\mathcal{N}} \cdot {}^{\mathrm{IN}}\mathbf{C} \cdot \vec{\mathcal{N}}\right) = 0. \tag{43}$$

The application of the Rice bifurcation criterion requires the computation of the in-plane macroscopic tangent modulus ${}^{\mathrm{IN}}\mathbf{B}$. For such computation, Zhu et al. (2022) have compared three numerical techniques: the perturbation technique, the condensation technique, and the fluctuation technique, and they have concluded that the condensation method is the most reliable and efficient compared to the other ones. Hence, this technique is employed to compute the macroscopic tangent modulus in this study. The main steps of this technique are summarized as below:

- Output the elementary stiffness matrices $\mathbf{K}_{el}$ corresponding to all of the finite elements for each computation time increment using the ABAQUS keyword 'Element Matrix Output'.
- Assemble the global stiffness matrix $\mathbf{K}$ from the elementary matrices $\mathbf{K}_{el}$ using the connectivity of the different nodes of the elements.
- Partition the global stiffness matrix $\mathbf{K}$ into four submatrices $\mathbf{K}_{aa}$, $\mathbf{K}_{ab}$, $\mathbf{K}_{ba}$ and $\mathbf{K}_{bb}$, where $a$ is the set of nodes in the interior and

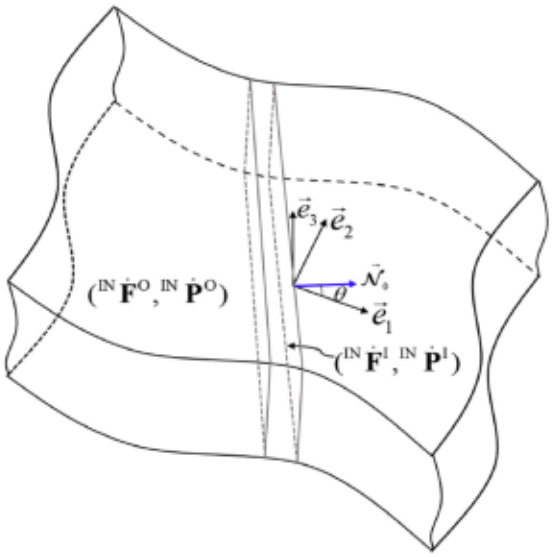


**Fig. 3.** Schematic of the Rice bifurcation criterion.

$b$ is the set of nodes on the boundary of the unit cell:

$$\mathbf{K} = \begin{bmatrix} \mathbf{K}_{aa} & \mathbf{K}_{ab} \\ \mathbf{K}_{ba} & \mathbf{K}_{bb} \end{bmatrix}. \tag{44}$$

- Construct the projection matrices $\mathbb{Q}$ and $\mathbb{H}$ according to the procedure developed in Zhu et al. (2022).
- The macroscopic tangent modulus $\mathbf{B}$ is computed by the following relation:

$$\mathbf{B} = \frac{1}{|\mathcal{V}_0|}\mathbb{Q}\cdot\left[\mathbb{H}\cdot\left(\mathbf{K}_{bb} - \mathbf{K}_{ba}\cdot\mathbf{K}_{aa}^{-1}\cdot\mathbf{K}_{ab}\right)\cdot\mathbb{H}^T\right]^{-1}\cdot\mathbb{Q}^T. \tag{45}$$

- The index form of the in-plane macroscopic tangent modulus ${}^{\mathrm{IN}}\mathbf{B}$ is given by:

$$\forall i,j,k,l = 1,2 : {}^{\mathrm{IN}}B_{ijkl} = B_{ijkl} - \frac{B_{ij33}B_{33kl}}{B_{3333}}. \tag{46}$$

This condensation technique is implemented in a set of Python codes. For more details about the foundation and the numerical implementation of this technique, interested readers can refer to Zhu et al. (2020a,b, 2022).

## 3. Results and discussions

### 3.1. Material data

The unit cell should contain a sufficient number of grains to embody essential microscopic features of the microstructure, and to statistically represent the effective mechanical behavior of the studied material in overall. It has been found in several previous contributions that 125 grains are quite sufficient to accurately represent the microstructure of the studied materials (Lim et al., 2019; Zhou et al., 2019). As a result, in the majority of the simulations presented in this work, polycrystalline aggregates composed of 125 FCC grains are used. The effect of grain morphology on the ductility limits is investigated using three different grain shapes: cube, random and elongated, as shown in Figs. 4(a)–4(c). Furthermore, to analyze the impact of the initial crystallographic orientation on the numerical predictions, three crystallographic textures are employed: random, cube ($\{001\}\langle 100\rangle$, $\varphi_1 = 0°$, $\phi = 0°$, $\varphi_2 = 0°$), and copper ($\{\bar{2}11\}\langle 111\rangle$, $\varphi_1 = 90°$, $\phi = 35°$, $\varphi_2 = 45°$), as illustrated in Fig. 5 (using the notation convention adopted in Raabe and Roters, 2004). In the majority of the simulations performed with cube and copper textures, the scatter width of the Gaussian distribution of the crystallographic orientations $\omega_0$ is set to 15°, which can be considered as a realistic value as reported by several Refs. (Yoshida et al., 2007, among others). For the sake of brevity, in the subsequent investigations and figures, morphological (resp. crystallographic) texture will be designated by the type of the texture followed by the word 'morph.' (resp. 'orien.'). For instance, aggregate with random distribution of crystallographic orientations will be denoted 'random orien.'.

Unless explicitly stated otherwise, the elastic and isotropic hardening parameters used in the FLD predictions are those given in Table 1. These parameters are taken from Yoshida and Kuroda (2012) and Tadano et al. (2013).

**Table 1**
Elasticity and hardening parameters.

| $E$ (GPa) | $\nu$ | $\tau_0$ (MPa) | $h_0$ (MPa) | $n$ | $\kappa_{HP}$ (MPa (mm)$^{1/2}$) |
|---|---|---|---|---|---|
| 65 | 0.3 | 40 | 390 | 0.1 | 0 |

**Table 2**
Number of finite elements for each configuration of mesh and grain morphology.

| | Cube morph. | Random morph. | Elongated morph. |
|---|---|---|---|
| Mesh_1 | 1000 | 1728 | 1728 |
| Mesh_2 | 3375 | 5832 | 5832 |
| Mesh_3 | 8000 | 12 167 | 12 167 |
| Mesh_4 | 15 625 | 24 389 | 24 389 |

### 3.2. Mesh sensitivity study

To determine the adequate number of finite elements required to discretize the unit cells, a mesh sensitivity study is carried out by simulating uniaxial tensile tests applied on several polycrystalline aggregates. In this aim, each aggregate is discretized by four different FE meshes as presented in Table 2. A random orien. (Fig. 5(a)) is used for each numerical test. The simulations of this section are performed on a cluster with 2.10 GHz of CPU frequency and 8 cores. Figs. 6(a) to 6(c) plot the equivalent macroscopic stresses (von Mises yield surface) and the relative errors versus the equivalent macroscopic strain for the different configurations of meshes and grain morphologies. The equivalent macroscopic stress and strain are defined in terms of the macroscopic principal stresses (resp. strains) $\Sigma_1, \Sigma_2, \Sigma_3$ (resp. $E_1, E_2, E_3$) as follows:

$$\Sigma_{eq} = \frac{\sqrt{2}}{2}\sqrt{\left(\Sigma_1-\Sigma_2\right)^2+\left(\Sigma_2-\Sigma_3\right)^2+\left(\Sigma_3-\Sigma_1\right)^2};$$
$$E_{eq} = \frac{\sqrt{2}}{3}\sqrt{\left(E_1-E_2\right)^2+\left(E_2-E_3\right)^2+\left(E_3-E_1\right)^2}. \tag{47}$$

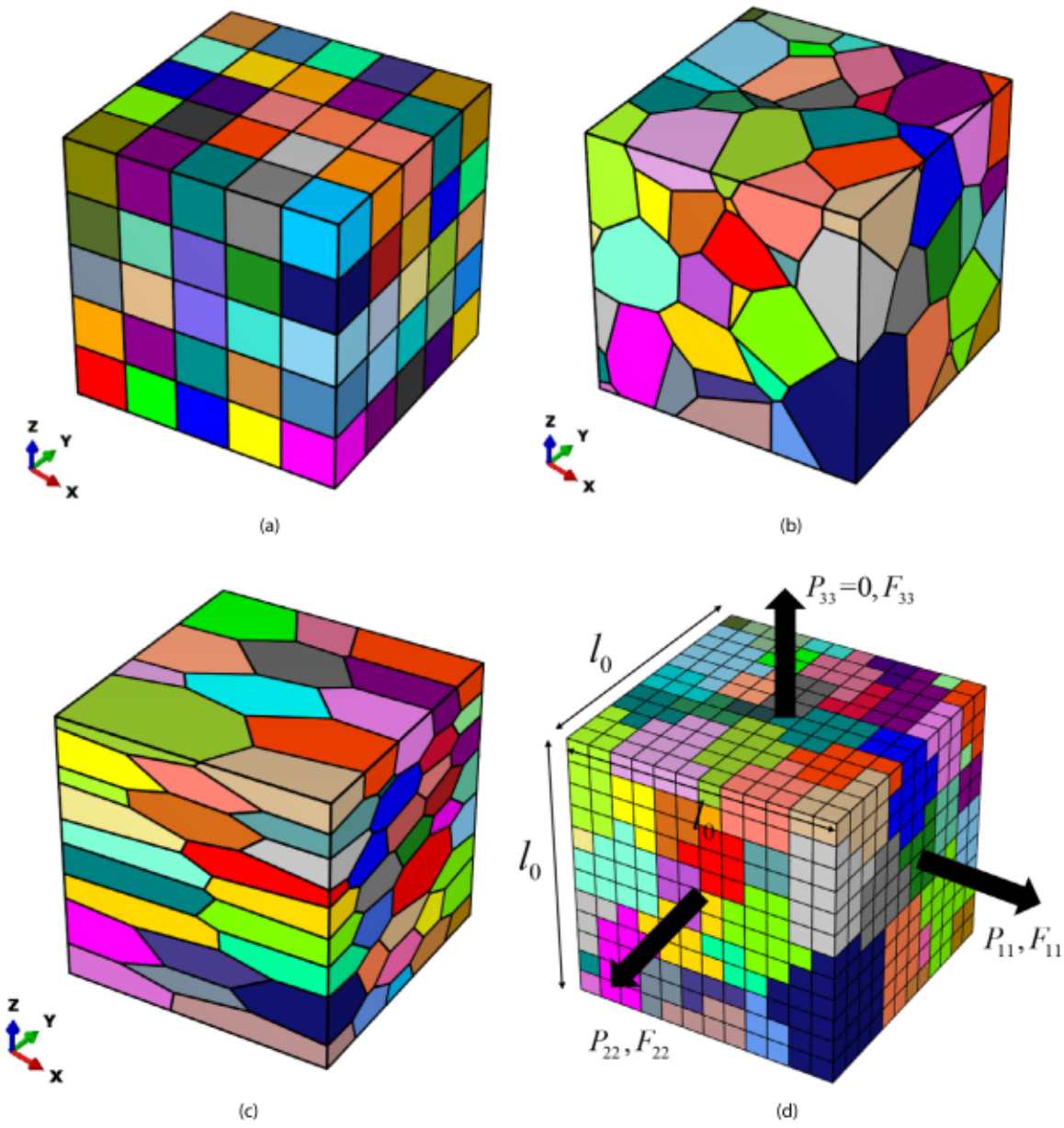


**Fig. 4.** Description of the polycrystalline aggregates: (a) aggregate with cube morph.; (b) aggregate with random morph.; (c) aggregate with elongated morph.; (d) finite element mesh and the applied macroscopic loading.

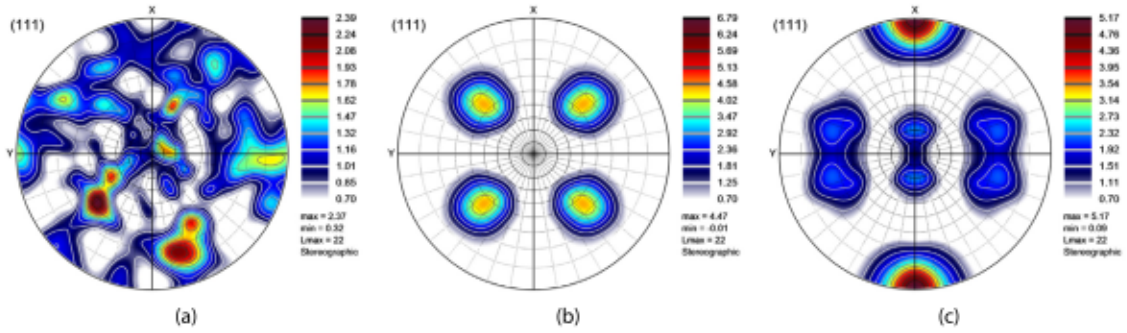


**Fig. 5.** (111) pole figures of the initial crystallographic textures with 125 orientations generated and plotted by the ATEX software: (a) random orien.; (b) cube orien.; (c) copper orien.

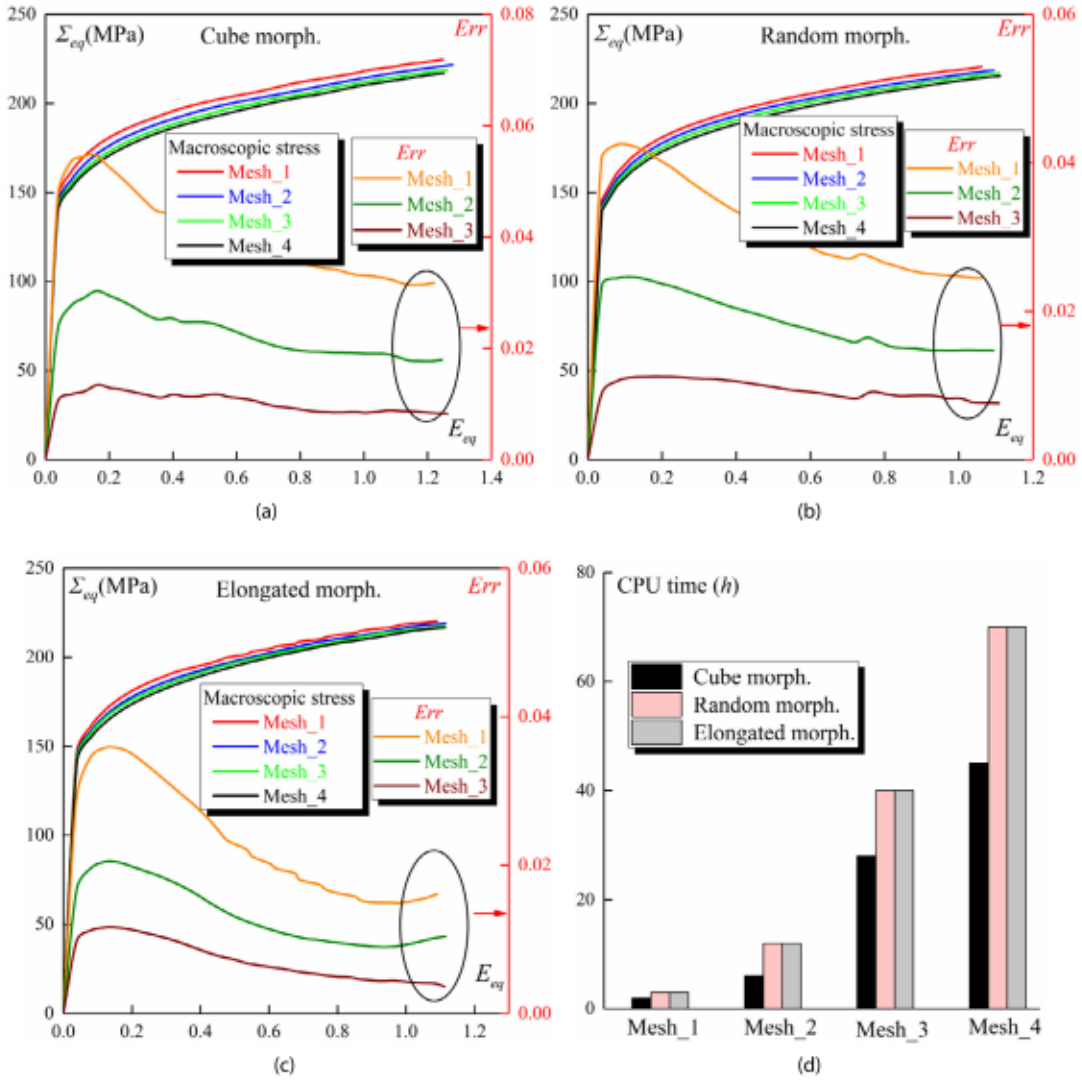


**Fig. 6.** Mesh sensitivity study: evolution of the equivalent macroscopic stress and relative error as a function of the equivalent macroscopic strain for aggregates with: (a) cube morph.; (b) random morph.; (c) elongated morph.; (d) study of the CPU time.

The macroscopic stress relative error is defined as:

$$Err = \frac{\Sigma_{eq}^{Mesh\_i} - \Sigma_{eq}^{Mesh\_4}}{\Sigma_{eq}^{Mesh\_4}}; i = 1, 2, 3, 4. \tag{48}$$

As clearly shown in Figs. 6(a) to 6(c), the stress–strain curves are almost insensitive to the finite element number. Indeed, the relative error $Err$ is always lower than 6% for all the meshes, regardless of the grain morphology. Furthermore, this relative error decreases with the increase of the element number (from Mesh_1 to Mesh_3). The CPU time required for all of these simulations is plotted in Fig. 6(d). One can observe that with the increase of the element number, the CPU time significantly increases. The computational effort of the CPFEM-based framework for Mesh_1 is nearly 23 times less than for Mesh_4. To balance the requirements in terms of computational efficiency and simulation accuracy, and also to avoid grain morphology distortion (particularly for grains with small size), Mesh_2 is adopted for the different grain morphologies in the subsequent numerical investigations.

### 3.3. Effect of initial crystallographic texture

#### 3.3.1. Effect of the type of initial crystallographic texture

To investigate the effect of the type of initial crystallographic texture on localized necking, as detected by the Rice bifurcation criterion, the evolution of the cubic root of the minimum of the determinant of the macroscopic acoustic tensor $\vec{\mathcal{N}} \cdot {}^{\mathrm{IN}}\mathbf{C} \cdot \vec{\mathcal{N}}$ as a function of the macroscopic strain component $E_{11}$, is reported in Fig. 7 for polycrystalline aggregates characterized by different grain morphologies and for strain paths defined by $\rho = -0.5, \rho = 0$, and $\rho = 1$. Strain localization occurs when the minimum of the determinant of the macroscopic acoustic tensor reaches zero, which is marked by solid circles in Fig. 7. One can observe that, for the case of cube morph. and uniaxial tensile state ($\rho = -0.5$), random orien. gives the largest bifurcation limit strain, followed by copper orien. and then cube orien. On the other hand, for random and elongated morph. and uniaxial tensile state, cube and copper orien. yield the same value of limit strain, which is again lower than that obtained for random orien.. For the plane strain tensile state ($\rho = 0$), the effects of crystallographic texture are rather small whatever the adopted morphology. Additionally, for the equibiaxial tensile state ($\rho = 1$), the predicted limit strains are significantly affected by the type of initial crystallographic and morphological textures. For instance, random orien. leads to almost the same magnitude of limit strain for cube and elongated morph., while the predicted magnitude is lower for random morph. Also, the limit strains corresponding to cube orien. are largest for random and elongated morph. As to copper orien., it provides the same level of limit strain for cube and random morph., while the predicted level is lower for elongated morph.

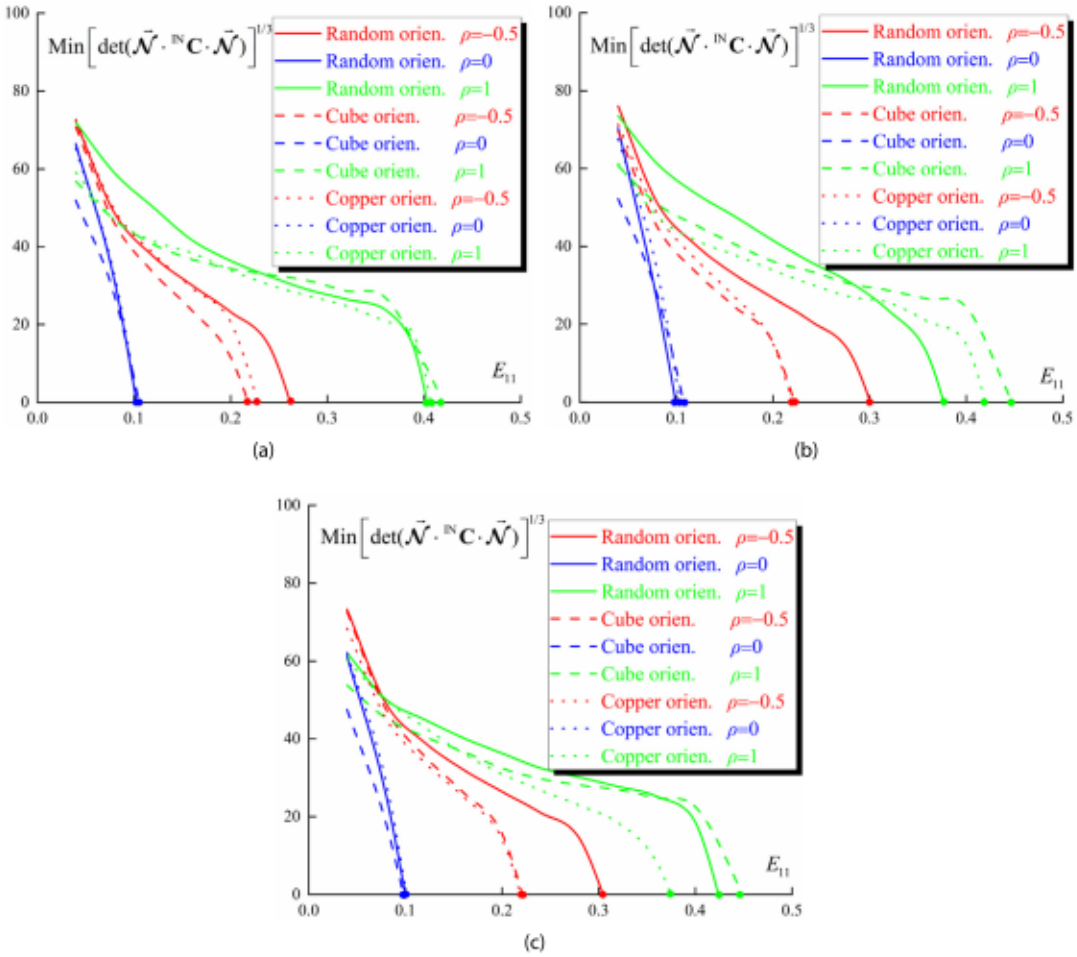


**Fig. 7.** Effect of the type of initial crystallographic texture on the evolution of the cubic root of the minimum of the determinant of the macroscopic acoustic tensor $\vec{\mathcal{N}}\cdot{}^{IN}\mathbf{C}\cdot\vec{\mathcal{N}}$ for $\rho=-0.5$, $\rho=0$, and $\rho=1$ for: (a) cube morph.; (b) random morph.; (c) elongated morph.

To investigate the effect of initial crystallographic texture on the ductility limits for the whole range of strain paths, the forming limit diagrams corresponding to different polycrystalline aggregates are plotted in Fig. 8. As expected, the impact of crystallographic texture is very small for negative strain paths. This observation is consistent with classical trends obtained in the literature according to which the ductility limit in this range of negative strain paths is only dependent on hardening parameters (Zhu et al., 2020b). Moreover, for the plane-strain tensile state ($\rho = 0$), the different textures provide almost the same level of limit strain whatever the grain morphology. However, the right-hand side of the forming limit diagrams is highly dependent on the anisotropic behavior, which is mainly related to the initial texture and its evolution during plastic deformation. One can observe from Fig. 8 that the cube orien. yields globally the largest formability for $\rho > 0$, followed by random orien., and then copper orien. Accordingly, the cube orien. leads to significant improvement in terms of formability. This is due to the fact that cube orien. is usually developed during the annealing process. Nakamachi et al. (2002) have confirmed, for the case of A5052-H34 aluminum alloy, that this process allows delaying plastic strain localization and thus improving formability. These results also confirm the earlier trends published in Kuroda (2005, 2007), Yoshida et al. (2007) and Yoshida and Kuroda (2012), where the Taylor multiscale model has been coupled with the Marciniak–Kuczynski approach (Marciniak and Kuczyński, 1967) for the prediction of the formability limits of some typical FCC polycrystalline aggregates. In addition, Fig. 8 highlight the impact of grain morphology on the predicted limit strains. A deeper analysis of the effect of grain morphology will be carried out in Section 3.4.

To further illustrate the localization of plastic deformation for the different crystallographic and morphological textures, the distribution of the accumulated dislocation density $\rho_{total}$ is plotted for strain-path ratio $\rho = -0.5$ at the onset of bifurcation in Fig. 9. The accumulated dislocation density is determined by adding the dislocation densities $\rho^{\alpha}$ of all the slip systems ($\rho_{total} = \sum_{\alpha=1}^{N_s} \rho^{\alpha}$). Following the work of Adam et al. (2018) and Patil et al. (2021), the dislocation densities $\rho^{\alpha}$ are back-calculated from the critical resolved shear stress $\tau_c^{\alpha}$ using the Taylor equation as follows[1]:

$$\forall \alpha = 1, \ldots, N_s \; : \; \rho^{\alpha} = \left(\frac{\tau_c^{\alpha}}{A\mu b}\right)^2, \tag{49}$$

where $A$ is a material constant, which takes into account average strength of the dislocation interactions, $b$ is the Burgers vector, and $\mu$ is the shear modulus computed as $\mu = E/2(1+\nu)$. Material parameters used for the dislocation density computation are provided in Table 3. Based on the trends observed in Fig. 9, one can conclude that the relatively high values of accumulated dislocation densities are distributed

[1] In fact, this method underestimates the dislocation densities. Hence, a better alternative to predict the dislocation densities should take into account the dislocation evolution equations and incorporated into the physical-based hardening. In this regard, one can quote Jeong and Voyiadjis (2022), where the statistically stored dislocations (SSDs) and geometrically necessary dislocations (GNDs) are considered.

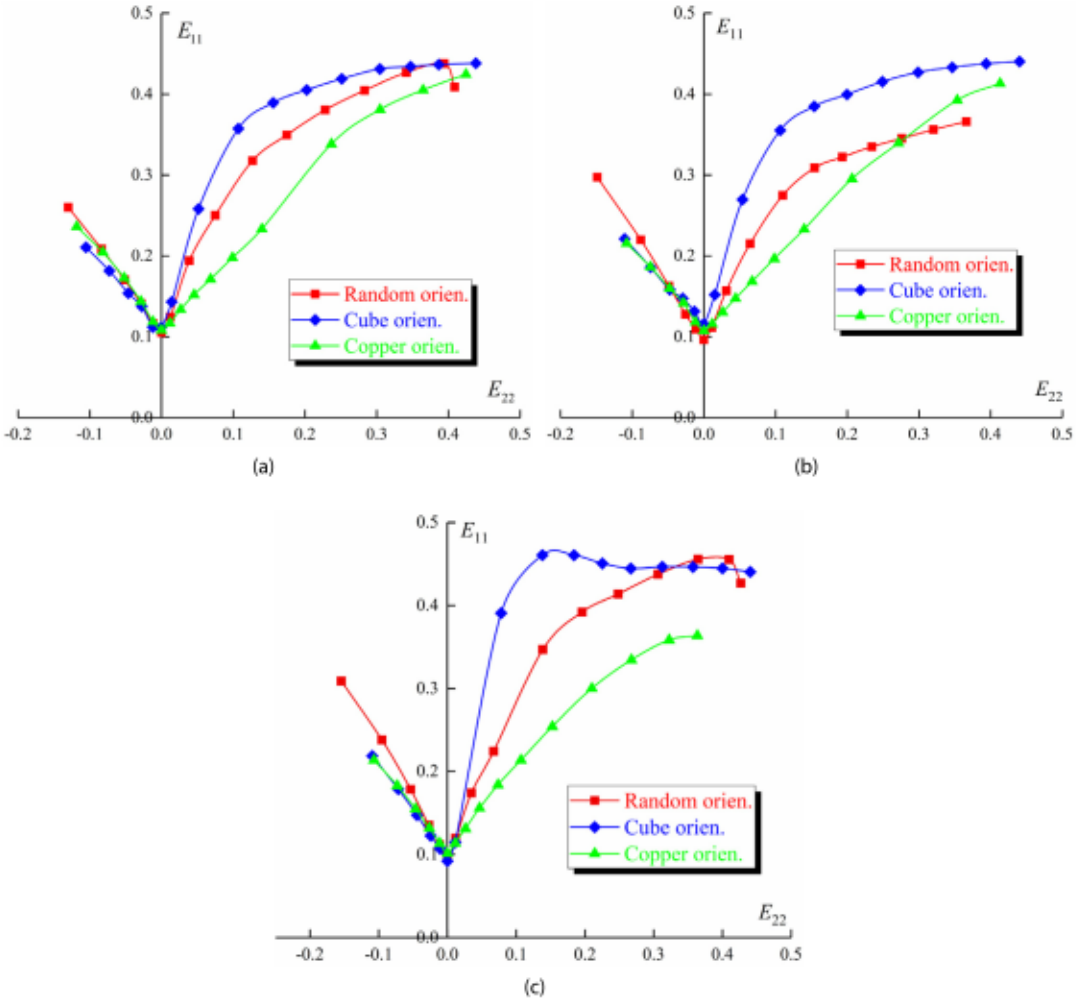


**Fig. 8.** Effect of initial crystallographic texture on the FLDs for: (a) cube morph.; (b) random morph.; (c) elongated morph.

**Table 3**
Material parameters for dislocation density computation.

| $A$ | $\mu$ (GPa) | $b$ (mm) |
|---|---|---|
| 0.5 | 25 | $2.86 \times 10^{-7}$ |

at the grain boundaries. Furthermore, it is found that these high total dislocation densities corroborate the ductility limit predictions.

In addition, the crystallographic texture evolution is investigated in this section. In order to address this point, the crystallographic orientations are obtained as outputs from the UMAT and plotted in the form of (111) pole figures by ATEX software. For the sake of brevity, only the simulation results for the random crystallographic texture (for aggregate with random morph.) are presented in Fig. 10 for strain-path ratios $\rho = -0.5$ and $\rho = 1$, where the evolution of texture with the increase of the macroscopic strain $E_{11}$ is plotted until the detection of bifurcation. Comparing Fig. 10 with Fig. 5(a) (initial random texture), one can see that pronounced intensity is observed in the X direction for uniaxial tensile state ($\rho = -0.5$) with the increase of the macroscopic strain component $E_{11}$. Also, one can see that the random texture evolves into the X–Y plane for the equibiaxial tensile state ($\rho = 1$) with the increase of the macroscopic strain component $E_{11}$. Moreover, the intensity of the pole figures for each strain path becomes more pronounced after plastic strain localization, as compared to the initial one.

### 3.3.2. *Effect of the spatial distribution of crystallographic orientations*

In order to explore the effect of the spatial distribution of crystallographic orientations on the forming limit diagrams, three random textures are considered: random orien. presented in Fig. 5(a), random orien. 2, and random orien. 3. Random orien. 2 and random orien. 3 are generated from random orien., where the Euler angles are kept the same, while the overall texture is randomly shuffled and assigned otherwise to different constituent grains. This change in the assignment of crystallographic orientations leads to a modification of the interactions between the neighboring grains (as the grains will have different neighbors) and then to a modification of the overall macroscopic behavior. It should be noted that the effect of the spatial distribution of crystallographic orientations cannot be detected if a mean-field multiscale scheme (such as the Taylor or the self-consistent model) is used to determine the overall mechanical behavior of the polycrystalline aggregate, as the interactions between grains are ignored. This aspect represents a major advantageous of the adopted CPFEM-based multiscale scheme as compared to more classical mean-field approaches. The effect of the spatial distribution of random textures on the forming limit diagrams for the different grain morphologies is analyzed through the FLDs of Fig. 11. It can be seen that no appreciable effects are noticed on the predicted limit strains from uniaxial tensile state ($\rho = -0.5$) to biaxial tensile state ($\rho = 0.5$). However, near the equibiaxial tensile state, the spatial

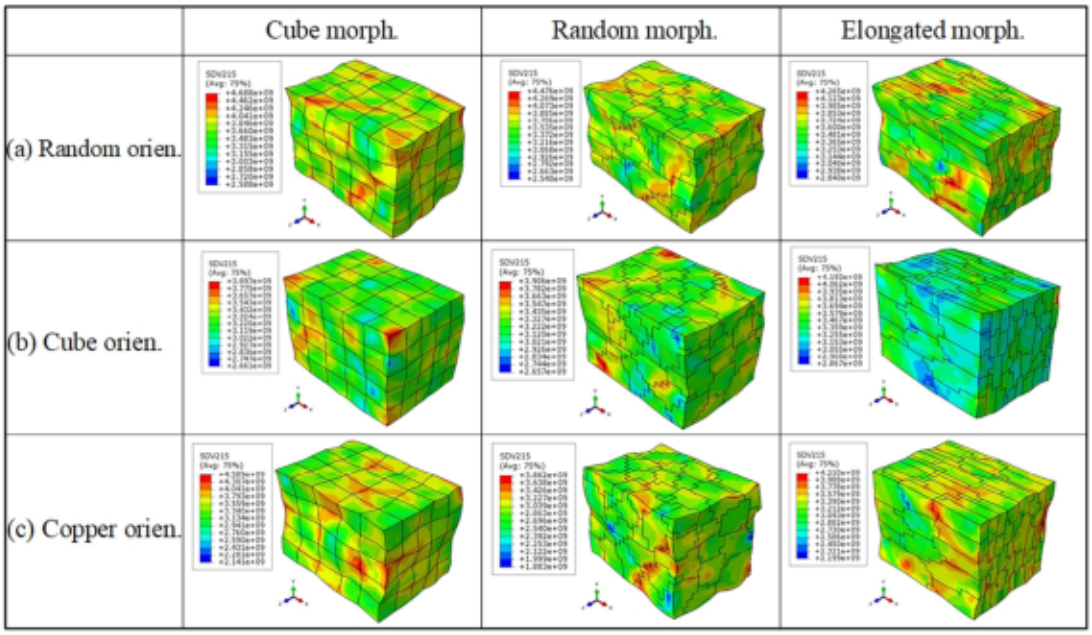


**Fig. 9.** Distribution of the accumulated dislocation density (unit: $mm^{-2}$) for the different crystallographic and morphological textures for strain-path ratio $\rho = -0.5$ at the onset of bifurcation. Grain boundaries are delineated by black lines.

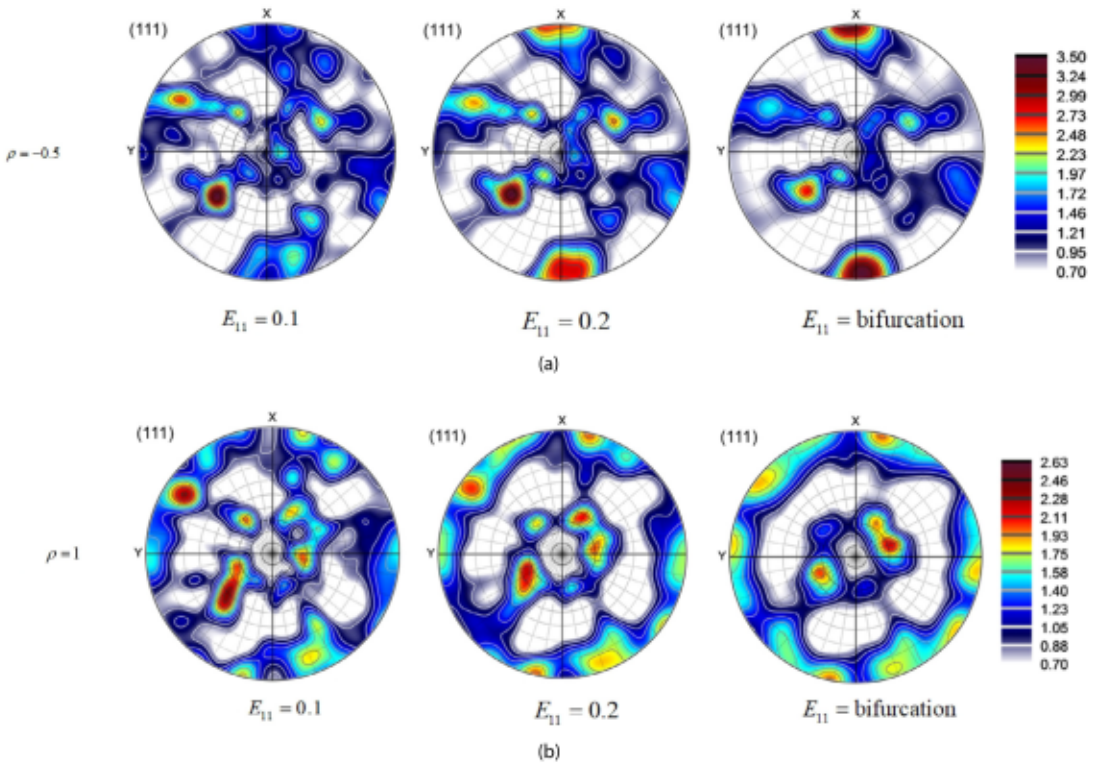


**Fig. 10.** Evolution of the random crystallographic texture (random morph.) with the macroscopic strain component $E_{11}$ until the detection of bifurcation for strain-path ratios: (a) $\rho = -0.5$; (b) $\rho = 1$.

distribution of random orien. shows a significant impact on the limit strain predictions. As aforementioned in Section 3.3.1, the left-hand side of the FLDs is mainly dependent on hardening parameters, which remain unchanged when the arrangement of crystallographic texture is modified. These results are quite expectable, as the redistribution of crystallographic orientations leads to a change in the plastic anisotropy of the polycrystalline aggregate, which affects the ductility limits near the equibiaxial tensile state. Similar conclusions have been obtained by Wu et al. (2007).

### 3.3.3. *Effect of the scatter width $\omega_0$ of the initial crystallographic texture*

To further investigate the effect of initial crystallographic texture on the forming limit diagrams, two copper crystallographic textures defined by two scatter widths ($\omega_0$ = 15° and 25°) are designed using

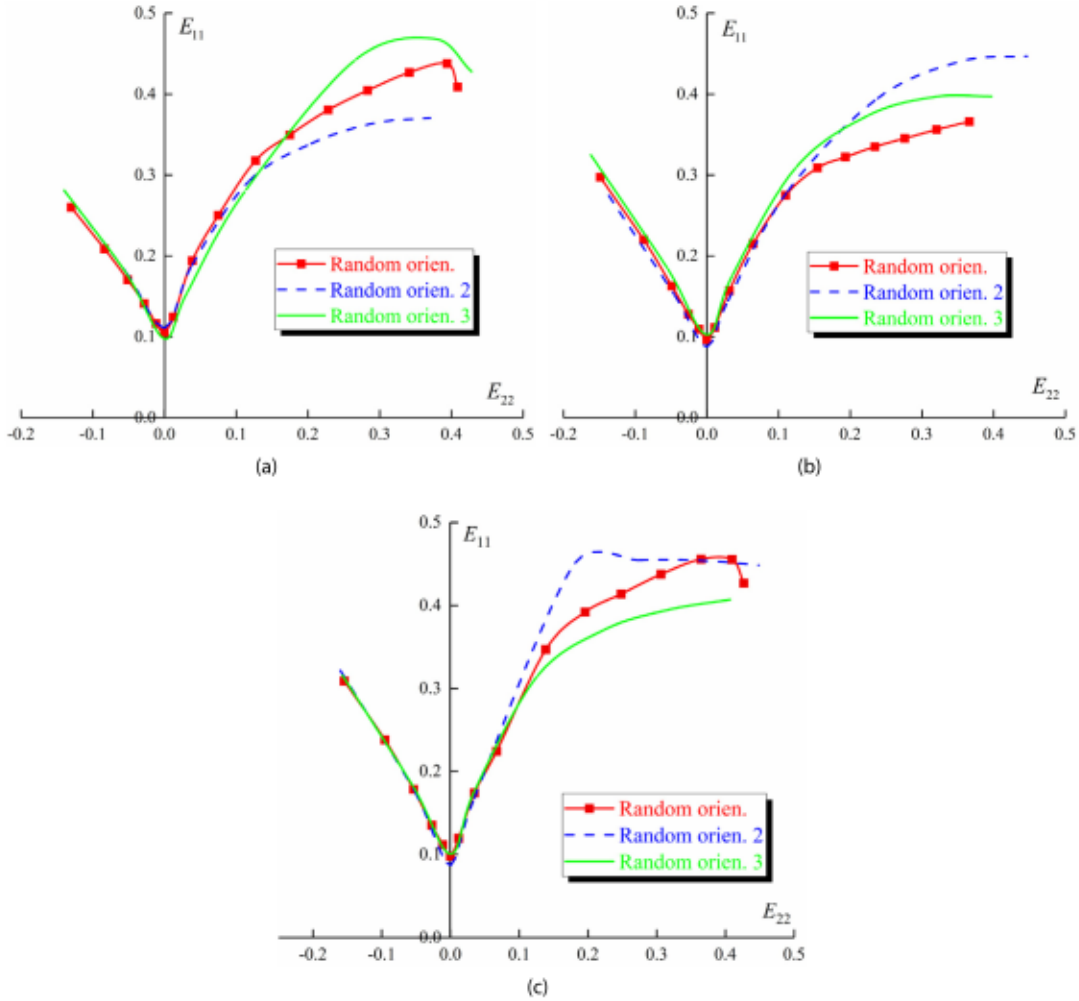


**Fig. 11.** Effect of the spatial distribution of random textures on the FLDs for: (a) cube morph.; (b) random morph.; (c) elongated morph.

the ATEX software. The $\varphi_2$ constant sections of the orientation distribution function (ODF) (with $0° \leq \varphi_2 \leq 85°$ and step $\Delta\varphi_2$ set to 5°) corresponding to these orientations are shown in Fig. 10. More details about the procedure used to generate these ODFs are provided in Helming et al. (1994), Raabe and Roters (2004) and Chandola et al. (2018). It is clearly shown in Fig. 12 that, with the decrease of the scatter width $\omega_0$, the copper crystallographic texture becomes stronger, as the distribution of grain orientation becomes more concentrated. As indicated in Fig. 12, the evolution of the copper orien. is expanded with the increase of the scatter width $\omega_0$. Accordingly, the resulting texture becomes closer to random orien. when it is defined by a large value of $\omega_0$ (Chandola et al., 2018). For the sake of brevity, we have only checked the case of cube morph. It is observed from Fig. 13 that with the increase of $\omega_0$, no significant differences are noticed on the left-hand side of the FLD. However, a low value of $\omega_0$ leads to a decrease in the forming limit strains in the range of positive strain paths, thus indicating an earlier onset of strain localization during plastic deformation. As expected, the FLD corresponding to random orien. sets an upper bound to those obtained for lower values of $\omega_0$. This result is in very good agreement with those reported in Yoshida et al. (2007) and confirms once again the major role played by the initial crystallographic texture in the ductility limit prediction.

### 3.4. Effect of grain morphology

The effect of grain morphology on the mechanical response is firstly studied in this section. For this purpose, polycrystalline aggregates with the three grain morphologies are submitted to uniaxial tension along the X direction. The random crystallographic texture (Fig. 5(a)) is employed for these aggregates. Fig. 14 shows the effect of grain morphology on the equivalent macroscopic stress–strain response. As can be seen from this figure, the equivalent macroscopic stress–strain response is almost insensitive to the grain morphology. This conclusion is consistent with the trends obtained in Nagra et al. (2018). Nevertheless, we believe that strong plastic anisotropy should be observed for polycrystalline aggregates with elongated morphology, and their mechanical response would be dependent on the direction of the applied loading.

In what follows, attention is focused on the effect of grain morphology on the predicted ductility limits. By analyzing the results of Fig. 15, the following comments can be drawn:

- Overall, the effect of grain morphology on the ductility limit predictions is almost negligible for negative strain paths. However, remarkable differences are observed in the range of positive strain paths due to the use of different grain shapes. This result can be traced back to fluctuations in micromechanical fields caused by grain interactions and grain morphology. These fluctuations have a significant impact on plastic anisotropy and texture evolution, which in turn play an important role in the prediction of localized necking, thus leading to different ductility levels for positive strain paths.
- By comparison with Fig. 8, it is clearly revealed that the effect of crystallographic texture on the ductility limit is more important than that of grain morphology.

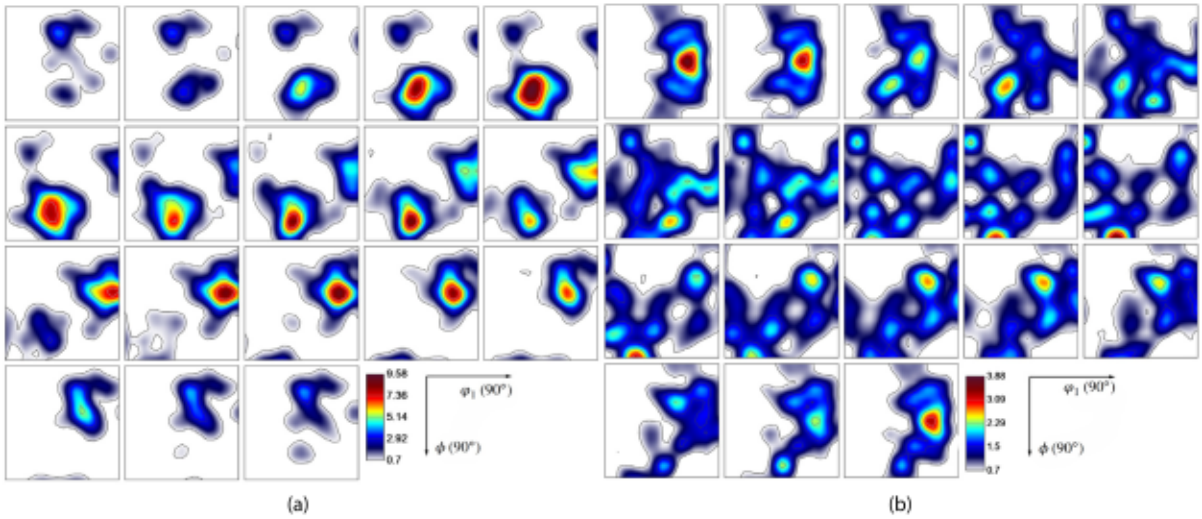


**Fig. 12.** $\varphi_2$ constant sections of the ODF (with $0° \le \varphi_2 \le 85°$ and $\Delta\varphi_2 = 5°$) corresponding to copper orien. for scatter width: (a) $\omega_0 = 15°$; (b) $\omega_0 = 25°$.

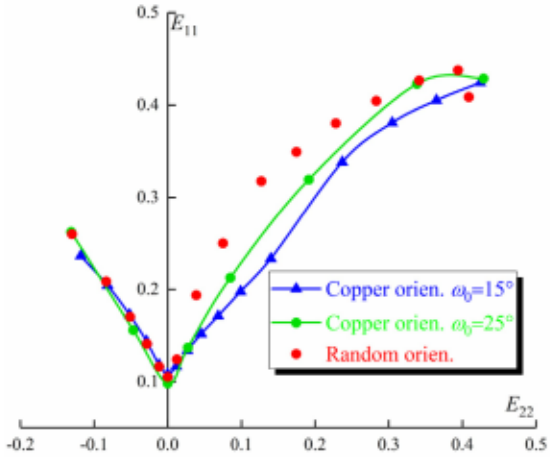


**Fig. 13.** Effect of the scatter width $\omega_0$ on the forming limit diagrams of polycrystalline aggregates with copper orien. and cube morph.

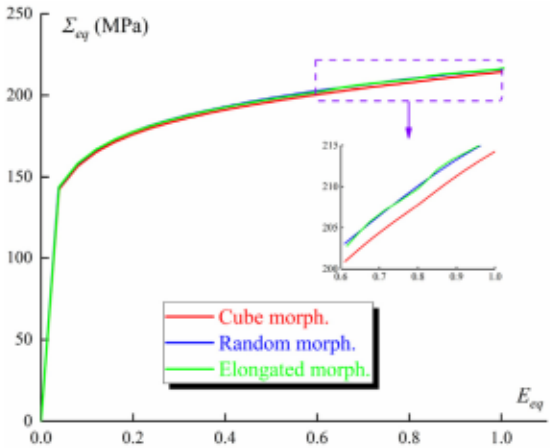


**Fig. 14.** Effect of grain morphology on the equivalent macroscopic stress–strain response under uniaxial tension along the X direction.

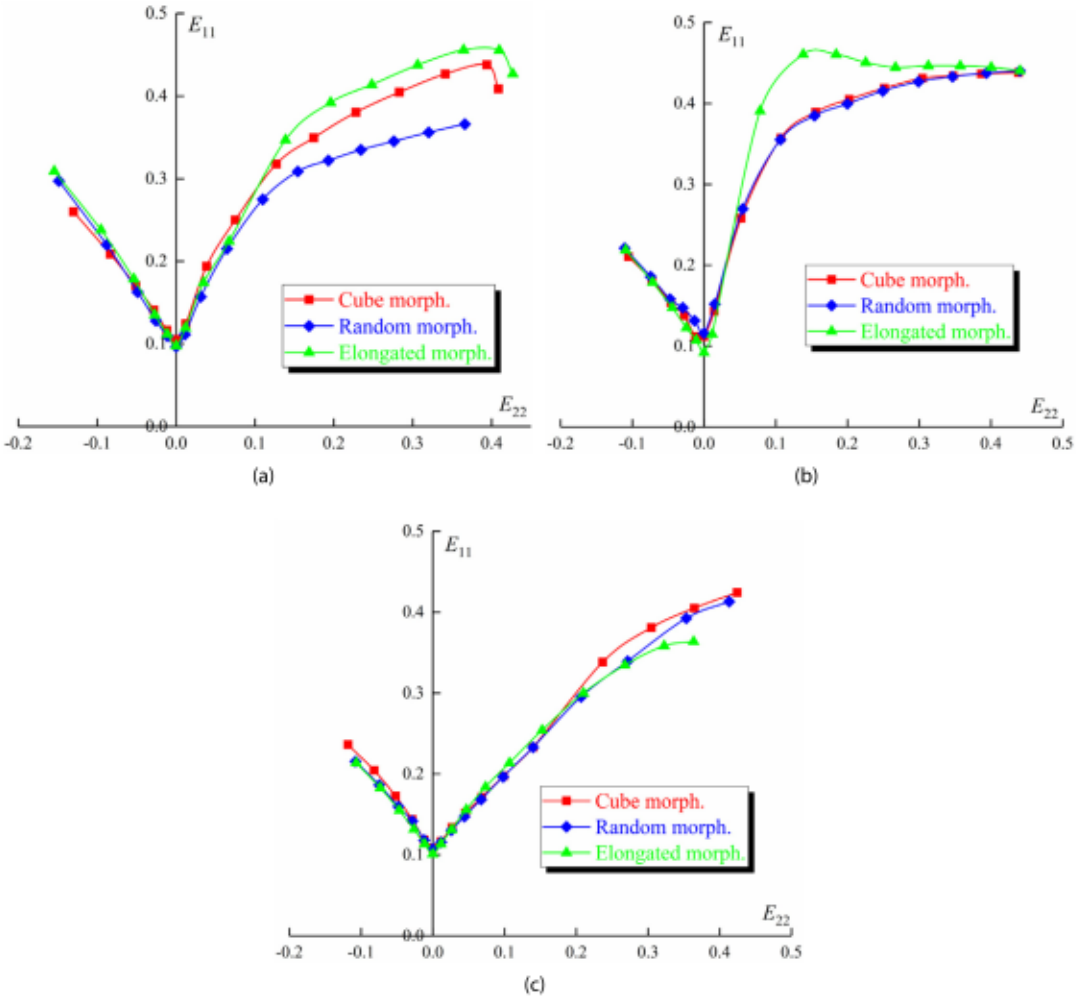


**Fig. 15.** Effect of morphological textures on the forming limit diagrams for: (a) random orien.; (b) cube orien.; (c) copper orien.

- For random orien., Fig. 15(a) suggests that elongated morph. leads to an improvement in terms of formability, in comparison to cube morph. and random morph.
- For cube orien, the predicted limit strains are nearly identical for cube and random morph., while elongated morph. yields higher limit strains in the range of positive strain paths ($\rho > 0$), as shown in Fig. 15(b).
- For copper orien., on the whole, the effect of grain morphology on the limit strains is almost indistinguishable (Fig. 15(c)). In other words, the copper orien. leads to practically the same FLD for cube, random, and elongated morph.

### 3.5. Effect of grain size and sheet thickness

In order to characterize the size effects, the concept of thickness-to-grain size ratio ($t/d$) is commonly adopted in the literature Amelirad and Assempour (2019). In this section, we investigate two main size effects on the predicted ductility limits: by varying the grain size $d$ for constant thickness, and by varying the unit cell thickness for a fixed grain number. For the sake of brevity, we have only considered unit cells with random morph. and random orien.

#### 3.5.1. Effect of grain size

To investigate the effect of the grain size on the ductility limits, the microscopic Hall–Petch constant $\kappa_{HP}$ is set to 6.325 MPa $(\text{mm})^{1/2}$ (Farhat et al., 1996), while the other parameters are kept to their values specified in Table 1. To capture the grain size dependence, unit cells with grain size respectively equal to 0.4095 mm, 0.2401 mm, 0.1518 mm and 0.1211 mm are considered, as shown in Fig. 16(a). Fig. 16(b) presents the evolution of the equivalent macroscopic stress as a function of the equivalent macroscopic strain under uniaxial tension loading for different grain sizes. The results reveal that the mechanical strength is strongly related to the grain size (i.e., the mechanical strength increases when the grain size decreases), showing a well-known phenomenon of 'the smaller the stronger' (Zhang et al., 2023, among others). Fig. 16(c) displays the equivalent macroscopic yield stress in terms of $1/\sqrt{d_{eff}}$ at equivalent macroscopic strain offsets of 2%, 5% and 10% with different grain sizes. As can be observed, a slight increase was found in the slopes of the linear fit: 27.525, 32.61, and 35.682 MPa $(\text{mm})^{1/2}$ for each strain offset. The predicted forming limit diagrams are plotted in Fig. 16(d). It is clearly revealed from this figure that the grain size effect on ductility becomes significant only for large values of strain-path ratio (i.e., for $\rho > 0.5$). By contrast, no significant differences in the predicted limit strains are observed for lower values of strain-path ratio (i.e., $\rho < 0.5$). Furthermore, the formability limits for large strain-path ratios (i.e., $\rho > 0.5$) increase with decreasing the grain size (i.e., increase in ratio $t/d$). This expected result confirms several experimental observations published in the literature (Xu et al., 2014, 2015).

#### 3.5.2. Effect of sheet thickness

The effect of sheet thickness on the ductility limits is investigated in the current subsection. For that purpose, three unit cells, noted AGS1, AGS2 and AGS3, are considered (Fig. 17(a)). For all of these unit cells, the total grain number $N_g$ is set to 125 and the lengths along the $X$

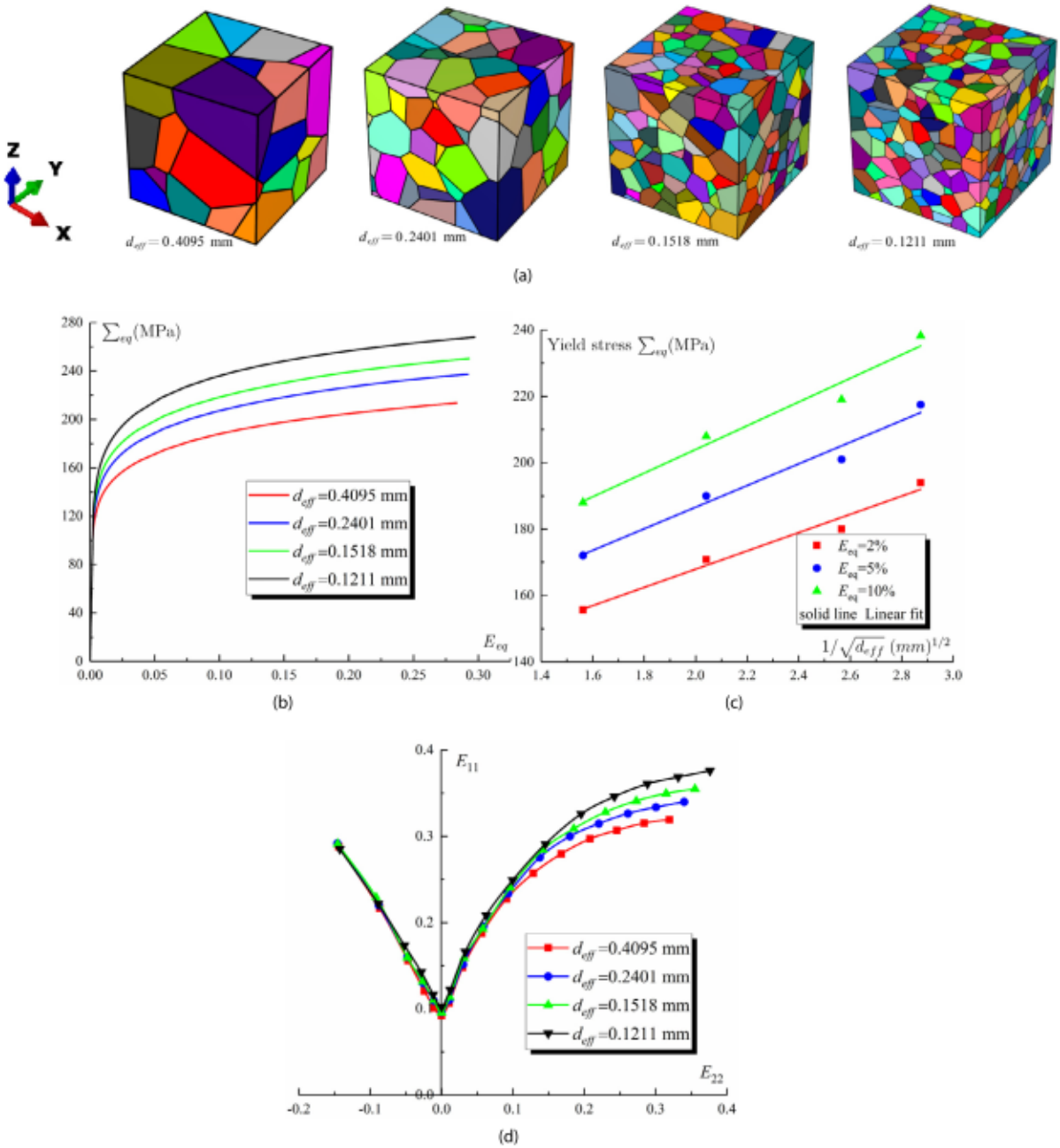


**Fig. 16.** Investigation of grain size effect on the FLD predictions: (a) unit cell models associated with different grain sizes; (b) evolution of the equivalent macroscopic stress as a function of the equivalent macroscopic strain curve for different grain sizes; (c) equivalent macroscopic yield stress at equivalent macroscopic strain offsets of 2%, 5% and 10% in terms of $1/\sqrt{d_{eff}}$ for different grain sizes; (d) corresponding predicted FLDs.

and $Y$ directions are kept equal to $l_0$, while the thickness $l_{0z}$ is varied from one unit cell to another as follows:

- AGS1: $l_{0z}/N_g = 1$ μm.
- AGS2: $l_{0z}/N_g = 4$ μm.
- AGS3: $l_{0z}/N_g = 8$ μm.

It is noted that the number of finite elements and the crystallographic texture are taken to be the same for these three unit cells. Fig. 17(b) plots the predicted forming limit diagrams for the three different unit cells. One can observe that with the increase in sheet thickness, the predicted limit strains increase for the whole range of strain-path ratios. This reveals that as the thickness-to-grain size ratio decreases, an individual grain plays an important role in the FLD prediction. Zhang et al. (2018) also reported that the fracture failure is little sensitive to thickness for configurations with a large ratio ($t/d \geq 6$), while significantly affected by thickness when $t/d \leq 3$. Tran et al. (2022) used the CPFEM approach in conjunction with the M–K model (Marciniak and Kuczyński, 1967) to investigate the size effect on the formability of ultra-thin ferritic stainless steel sheets. They found that the formability of ultra-thin steel sheets decreases with the increase in grain size (i.e., decrease in ratio $t/d$). Similar trends have been reported in the literature (Gau et al., 2007; Xu et al., 2014; Ma et al., 2016).

### 3.6. Comparison with the considère criterion

To illustrate the difference between diffuse and localized necking phenomena, the Considère criterion (Considère, 1885) is used to determine the occurrence of diffuse necking. It must be recalled that

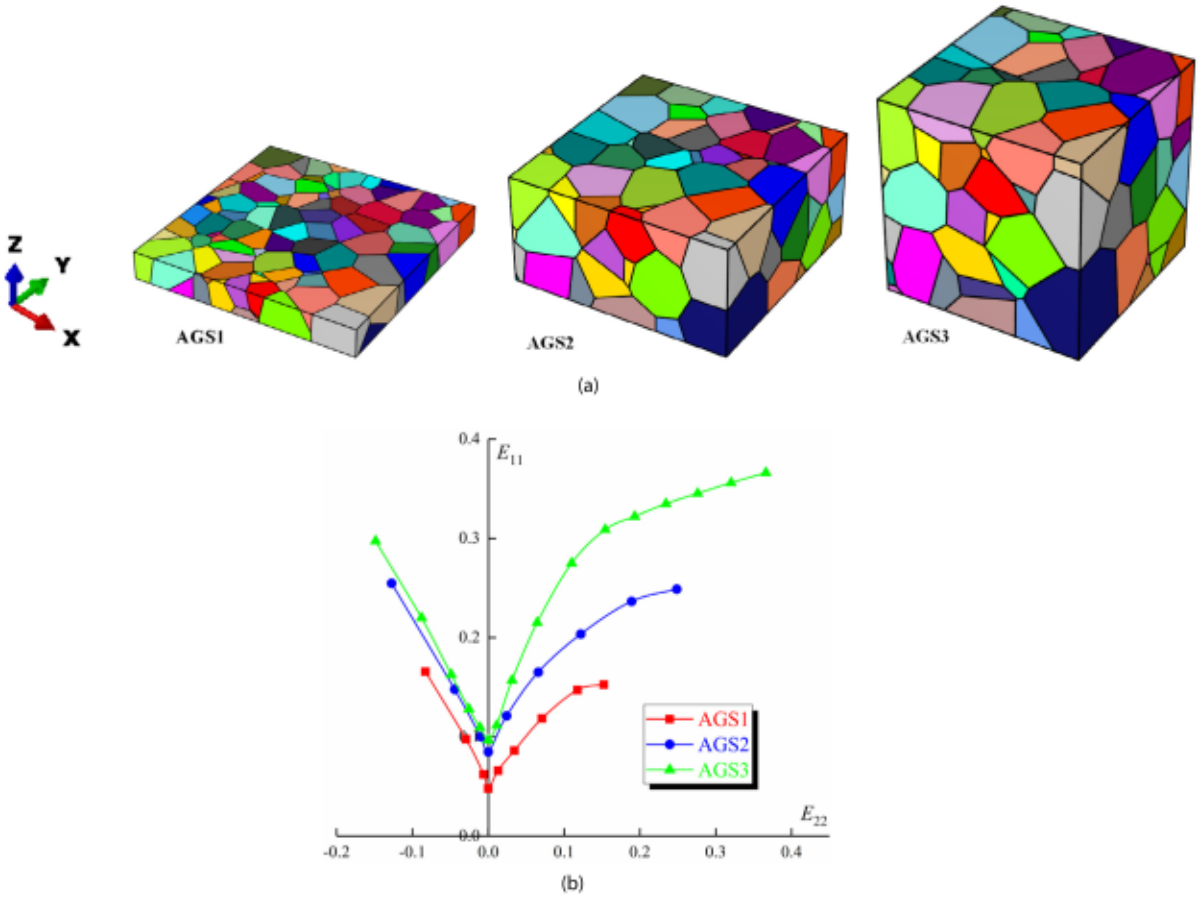


**Fig. 17.** (a) Three unit cell models of different sheet thicknesses with 125 grains; (b) corresponding forming limit diagrams.

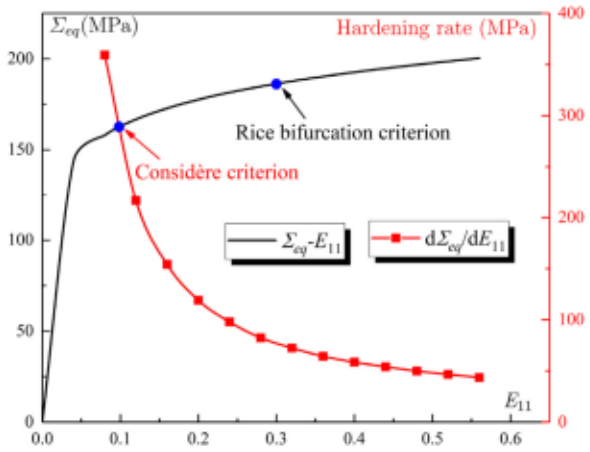


**Fig. 18.** Evolution of the macroscopic equivalent stress $\Sigma_{eq}$ and the hardening rate $d\Sigma_{eq}/dE_{11}$ as functions of the macroscopic strain component $E_{11}$ for uniaxial tension state with random orien. and morph.

this criterion is only applicable to uniaxial tension state and cannot provide a complete FLD; thereby, the result corresponding to the Rice bifurcation approach is only shown for strain path $\rho = -0.5$. For the sake of brevity, the random morph. with random orien. is considered in this section. Fig. 18 depicts the evolution of the macroscopic equivalent stress $\Sigma_{eq}$ and the hardening rate $d\Sigma_{eq}/dE_{11}$ as functions of the macroscopic strain component $E_{11}$ for uniaxial tension state. The predicted major limit strain $E_{11}$ is equal to 0.1 and 0.3 for Considère criterion and Rice bifurcation criterion, respectively (marked by blue points). This result confirms that diffuse necking occurs prior to localized necking.

## 4. Summary and concluding remarks

In this paper, a crystal plasticity finite element method has been developed to numerically predict the ductility limits of polycrystalline aggregates with FCC structure. For that task, the unit cell macroscopic behavior has been derived from that of the constituent single crystals on the basis of the periodic homogenization technique. The single crystal behavior follows a finite strain elastoplastic framework, where the plastic flow rule obeys the classical Schmid law. The crystal plasticity constitutive equations have been implemented within

**Table A.1**
The numbering of the crystallographic slip systems for FCC single crystals.

| $\alpha$ | 1 | 2 | 3 | 4 | 5 | 6 | 7 | 8 | 9 | 10 | 11 | 12 |
|---|---|---|---|---|---|---|---|---|---|---|---|---|
| $\sqrt{3}\vec{\mathbf{m}}_0^\alpha$ | $\begin{Bmatrix}1\\1\\1\end{Bmatrix}$ | $\begin{Bmatrix}1\\1\\1\end{Bmatrix}$ | $\begin{Bmatrix}1\\1\\1\end{Bmatrix}$ | $\begin{Bmatrix}-1\\1\\1\end{Bmatrix}$ | $\begin{Bmatrix}-1\\1\\1\end{Bmatrix}$ | $\begin{Bmatrix}-1\\1\\1\end{Bmatrix}$ | $\begin{Bmatrix}1\\-1\\1\end{Bmatrix}$ | $\begin{Bmatrix}1\\-1\\1\end{Bmatrix}$ | $\begin{Bmatrix}1\\-1\\1\end{Bmatrix}$ | $\begin{Bmatrix}1\\1\\-1\end{Bmatrix}$ | $\begin{Bmatrix}1\\1\\-1\end{Bmatrix}$ | $\begin{Bmatrix}1\\1\\-1\end{Bmatrix}$ |
| $\sqrt{2}\vec{\mathbf{n}}_0^\alpha$ | $\begin{Bmatrix}1\\-1\\0\end{Bmatrix}$ | $\begin{Bmatrix}1\\0\\-1\end{Bmatrix}$ | $\begin{Bmatrix}0\\1\\-1\end{Bmatrix}$ | $\begin{Bmatrix}1\\1\\0\end{Bmatrix}$ | $\begin{Bmatrix}1\\0\\1\end{Bmatrix}$ | $\begin{Bmatrix}0\\1\\-1\end{Bmatrix}$ | $\begin{Bmatrix}1\\1\\0\end{Bmatrix}$ | $\begin{Bmatrix}1\\0\\-1\end{Bmatrix}$ | $\begin{Bmatrix}0\\1\\1\end{Bmatrix}$ | $\begin{Bmatrix}1\\-1\\0\end{Bmatrix}$ | $\begin{Bmatrix}1\\0\\1\end{Bmatrix}$ | $\begin{Bmatrix}0\\1\\1\end{Bmatrix}$ |

ABAQUS/Standard finite element code via a user-defined material subroutine UMAT. Various morphological and crystallographic textures for thin metal sheets have been assessed to investigate their effects on ductility, with the ductility limits being determined by the Rice bifurcation criterion. The proposed CPFEM-based framework is particularly suitable to accurately study these aspects. Hereafter, some main conclusions are drawn and summarized as follows:

- The initial crystallographic texture (e.g., random, cube, or copper orien.) can significantly influence the ductility limits, especially in the range of positive strain-path ratios ($\rho > 0$).
- The grain morphology (e.g., cube, random, or elongated morph.) can greatly influence the predicted ductility limits. According to the results of this study, this behavior is mainly linked to the type of initial crystallographic texture.
- The effect of initial crystallographic texture on the ductility limit predictions is significantly more important than that of grain morphology.
- The numerical results reveal that the grain size has a remarkable effect on the formability of very thin metal sheets. Similar conclusions have been reported by other researchers in their experimental and numerical investigations.

## CRediT authorship contribution statement

**S. Zhou:** Writing – original draft, Software, Methodology, Investigation, Data curation. **M. Ben Bettaieb:** Writing – review & editing, Supervision, Software, Methodology, Investigation. **F. Abed-Meraim:** Writing – review & editing, Supervision, Software, Methodology.

## Declaration of competing interest

The authors declare that they have no known competing financial interests or personal relationships that could have appeared to influence the work reported in this paper.

## Data availability

No data was used for the research described in the article.

## Appendix A. Crystallographic slip systems for FCC single crystals

Table A.1 gives the numbering of the crystallographic slip systems for FCC single crystals. Each slip system is described by orthonormal vectors $(\vec{\mathbf{m}}_0^\alpha, \vec{\mathbf{n}}_0^\alpha)$.

## Appendix B. Integration algorithm

The constitutive equations at the single crystal scale are implemented within ABAQUS/Standard FE code through a user-defined material subroutine UMAT. In this implementation, the constitutive equations are integrated over the time interval of interest $I^\Delta = [t_0, t_0 + \Delta t]$ using an ultimate integration scheme. The family of ultimate algorithms has been initially introduced by Borja and Wren (1993) to integrate linear single crystal constitutive equations (linear hardening and small strain). More recently, this algorithm has been extended by Ben Bettaieb et al. (2012) to take into account more general non-linear behavior (non-linear hardening, finite strain, and finite rotation). The high performance and the robustness of the ultimate algorithm, compared to the well-known return-mapping one (Anand and Kothari, 1996) for the integration of rate-independent single crystal constitutive equations, has been emphasized by Akpama et al. (2016) through an extensive comparative study. Moreover, it has been proven in Akpama et al. (2016) that the explicit version of the ultimate algorithm is more efficient than the implicit one, since it yields quite accurate predictions with a reduced computation cost. Consequently, the explicit ultimate algorithm is adopted in the present study to integrate the single crystal constitutive equations. The concept of ultimate algorithm relies on the idea of partition of the time increment $I^\Delta$ into several sub-increments $I^{\delta_n} = [t_n, t_{n+1}]$ (where $t_{n=0} = t_0$). The size $\delta t_n = t_{n+1} - t_n$ of sub-increment $I^{\delta_n}$ is a priori unknown. It should be determined in such a way that the Schmid criterion remains fulfilled over $I^{\delta_n}$. By adopting this partition, the constitutive equations at the single crystal scale must be integrated over each time sub-increment $I^{\delta_n}$, and the different mechanical variables updated from one sub-increment to another.

The principal input of the UMAT is the velocity gradient $\mathbf{g}$, which is assumed to be constant over $\mathbf{I}^\Delta$ (hence, over $\mathbf{I}^{\delta_n}$), and is computed from $\mathbf{f}(t_0)$ and $\mathbf{f}(t_0 + \Delta t)$ by the following midpoint approximation:

$$\mathbf{g} = \left(\frac{\mathbf{f}(t_0 + \Delta t) - \mathbf{f}(t_0)}{\Delta t}\right) \cdot \left(\frac{\mathbf{f}(t_0 + \Delta t) + \mathbf{f}(t_0)}{2}\right)^{-1}. \tag{B.1}$$

To be consistent with the concept of implementation of constitutive equations in ABAQUS/Standard, let us introduce the co-rotational frame described by the rotation $\bar{\mathbf{r}}$ ($\neq \bar{\mathbf{r}}$) with respect to the fixed frame. The evolution of this rotation is defined by the following evolution law:

$$\dot{\bar{\mathbf{r}}} \cdot \bar{\mathbf{r}}^T = \mathbf{w}, \tag{B.2}$$

where $\mathbf{w}$ is the skew-symmetric part of the velocity gradient $\mathbf{g}$, as determined by Eq. (B.1). Vector and tensor quantities expressed in the co-rotational frame defined by rotation $\bar{\mathbf{r}}$ will be highlighted by a wavy line.

The other inputs of the UMAT are:

- The elasticity and hardening parameters.
- The rotation of the co-rotational frame $\bar{\mathbf{r}}$ and rotation of the crystallographic lattice related to the intermediate configuration $\bar{\mathbf{r}}$ at $t_n$.
- The Cauchy stress tensor expressed in the co-rotational frame $\tilde{\boldsymbol{\sigma}}$ at $t_n$.
- The slips $\gamma^\alpha$ and the critical shear stresses $\tau_c^\alpha$ (for $\alpha = 1, \ldots, 2N_s$) at $t_n$.

As outputs, the following unknowns need to be determined:

- The rotations $\bar{\mathbf{r}}$ and $\bar{\mathbf{r}}$ at $t_{n+1}$.
- The Cauchy stress tensor expressed in the co-rotational frame $\tilde{\boldsymbol{\sigma}}$ at $t_{n+1}$.
- The slips $\gamma^\alpha$ and the critical shear stresses $\tau_c^\alpha$ (for $\alpha = 1, \ldots, 2N_s$) at $t_{n+1}$.
- The consistent tangent modulus expressed in the co-rotational frame $\tilde{\mathbf{c}}^{ep}$ (i.e., **DDSDDE** matrix, using the ABAQUS terminology)

defined by the following expression:

$$\bar{\mathbf{c}}^{ep} = \frac{\partial \delta\bar{\boldsymbol{\sigma}}}{\partial \delta\bar{\boldsymbol{\varepsilon}}}, \tag{B.3}$$

where $\delta\bar{\boldsymbol{\sigma}}$ is the variation of $\bar{\boldsymbol{\sigma}}$ over the time sub-increment $I^{\delta_n}$, and $\delta\bar{\boldsymbol{\varepsilon}}$ is the integral of $\bar{\mathbf{d}}$ over the same sub-increment.

To clearly highlight the dependence with respect to time of the different quantities in the following algorithmic developments, a variable $\bullet$ evaluated at $t_n$ (resp. $t_{n+1}$) is denoted by $\bullet(t_n)$ (resp. $\bullet(t_{n+1})$). The rotation of the co-rotational frame $\bar{\mathbf{r}}(t_{n+1})$ can be determined from its counterpart at the beginning of the sub-increment $\bar{\mathbf{r}}(t_n)$ and $\mathbf{w}$ by integrating the differential Eq. (B.2) over $I^{\delta_n}$:

$$\bar{\mathbf{r}}(t_{n+1}) = e^{\delta t_n \mathbf{w}} \cdot \bar{\mathbf{r}}(t_n). \tag{B.4}$$

A quick analysis of the single crystal constitutive equations reveals that the computation of the slip rates $\dot{\gamma}^\alpha(t_n)$ for the different slip systems is sufficient to determine the evolution of the other single crystal mechanical variables over the current time sub-increment $I^{\delta_n}$, and especially their values at $t_{n+1}$ (namely, $\bar{\mathbf{r}}(t_{n+1})$, $\bar{\boldsymbol{\sigma}}(t_{n+1})$, $\gamma^\alpha(t_{n+1})$, $\tau_c^\alpha(t_{n+1})$, and $\bar{\mathbf{c}}^{ep}$).

To compute $\dot{\gamma}^\alpha(t_n)$ for all slip systems, let us introduce the set of potentially active slip systems $\mathcal{P}$ at $t_n$ defined as:

$$\mathcal{P} = \left\{ \alpha = 1, \dots, 2N_s \,:\, \tau^\alpha(t_n) - \tau_c^\alpha(t_n) = \bar{\boldsymbol{\sigma}}(t_n) : \mathbf{R}_0^\alpha(t_n) - \tau_c^\alpha(t_n) = 0 \right\}. \tag{B.5}$$

Considering the definition Eq. (B.5), the Schmid law defined by Eq. (32) may be reduced to the set of potentially active slip systems $\mathcal{P}$ (as the slip rates of the non-potentially active slip systems are obviously equal to zero):

$$\forall \alpha \in \mathcal{P} \,:\, \dot{\chi}^\alpha(t_n) = \dot{\tau}_c^\alpha(t_n) - \dot{\tau}^\alpha(t_n) \geq 0;\ \dot{\gamma}^\alpha(t_n) \geq 0;\ \dot{\chi}^\alpha(t_n)\dot{\gamma}^\alpha(t_n) = 0. \tag{B.6}$$

Making use of Eqs. (28), (29), (31), (33) and (34), $\dot{\chi}^\alpha(t_n)$ can be expressed as:

$$\begin{aligned}
\forall \alpha \in \mathcal{P} \,:\, \dot{\chi}^\alpha(t_n) = \dot{\tau}_c^\alpha(t_n) - \dot{\tau}^\alpha(t_n) &= \sum_{\beta\in\mathcal{P}} H^{\alpha\beta}\dot{\gamma}^\beta(t_n) - \dot{\bar{\boldsymbol{\sigma}}}(t_n) : \mathbf{R}_0^\alpha; \\
&= \sum_{\beta\in\mathcal{P}} H^{\alpha\beta}\dot{\gamma}^\beta(t_n) - \dot{\bar{\mathbf{d}}}^e(t_n) : \bar{\mathbf{c}}^e : \mathbf{R}_0^\alpha; \\
&= \sum_{\beta\in\mathcal{P}} H^{\alpha\beta}\dot{\gamma}^\beta(t_n) - \left( \bar{\mathbf{d}}(t_n) - \sum_{\beta\in\mathcal{P}} \dot{\gamma}^\beta(t_n)\mathbf{R}_0^\beta \right) : \mathbf{c}^e : \mathbf{R}_0^\alpha; \\
&= \sum_{\beta\in\mathcal{P}} A^{\alpha\beta}(t_n)\dot{\gamma}^\beta(t_n) - B^\alpha(t_n),
\end{aligned} \tag{B.7}$$

where matrix $\mathbf{A}(t_n)$ and vector $\mathbf{B}(t_n)$ are given by the following index forms:

$$\forall \alpha, \beta \in \mathcal{P} \,:\, A^{\alpha\beta}(t_n) = H^{\alpha\beta}(t_n) + \mathbf{R}_0^\alpha : \bar{\mathbf{c}}^e : \mathbf{R}_0^\beta;\ B^\alpha(t_n) = \mathbf{R}_0^\alpha : \bar{\mathbf{c}}^e : \bar{\mathbf{d}}(t_n). \tag{B.8}$$

Using Eqs. (B.7) and (B.8), the Schmid law given by Eq. (B.6) can be expressed in a matrix form more suitable to numerical implementation:

$$\forall \alpha \in \mathcal{P} \,:\, \begin{cases} \dot{\chi}^\alpha(t_n) = \sum\limits_{\beta\in\mathcal{P}} A^{\alpha\beta}(t_n)\dot{\gamma}^\beta(t_n) - B^\alpha(t_n) \geq 0; \quad \dot{\gamma}^\alpha(t_n) \geq 0; \\ \left( \sum\limits_{\beta\in\mathcal{P}} A^{\alpha\beta}(t_n)\dot{\gamma}^\beta(t_n) - B^\alpha(t_n) \right) \dot{\gamma}^\alpha(t_n) = 0. \end{cases} \tag{B.9}$$

As the components of $\mathbf{A}(t_n)$ and $\mathbf{B}(t_n)$ are determined at the beginning of the sub-increment $I^{\delta_n}$ (hence constant over $I^{\delta_n}$), the NLCP problem is transformed into a linear complementarity problem (LCP), as formulated by Eq. (B.9). This LCP can be easily solved by a combinatorial search procedure, identical to the one presented in Akpama et al. (2016), to compute the slip rates of the potentially active slip systems, and thus to distinguish the set of active slip systems $\mathcal{A}$ from the set of potentially active, but inactive slip systems $\mathcal{NA}$:

$$\begin{aligned}
&\mathcal{A} \cup \mathcal{NA} = \mathcal{P} \text{ and } \mathcal{A} \cap \mathcal{NA} = \varnothing, \\
&\forall \alpha \in \mathcal{A} \,:\, \dot{\gamma}^\alpha(t_n) > 0;\ \forall \alpha \in \mathcal{NA} \,:\, \dot{\gamma}^\alpha(t_n) = 0.
\end{aligned} \tag{B.10}$$

Once the slip rates of the potentially active slip systems computed, the size of the current sub-increment $I^{\delta_n}$ can be determined by satisfying the following conditions: $\delta t_n$ should be inferior or equal to $\Delta t$ and the Schmid criterion should be fulfilled for all slip systems over $I^{\delta_n}$. In view of Eq. (B.9), it is evident that the Schmid criterion is fulfilled for the potentially active slip systems. For the other systems ($\notin \mathcal{P}$), the following condition must be verified:

$$\forall \alpha \notin \mathcal{P} \,:\, \tau^\alpha(t_{n+1}) \leq \tau_c^\alpha(t_{n+1}). \tag{B.11}$$

By using the definitions of $\tau^\alpha$ and $\tau_c^\alpha$, the following relations can be readily obtained:

$$\forall \alpha \notin \mathcal{P} \,:\, \begin{cases} \tau^\alpha(t_{n+1}) = \tau^\alpha(t_n) + \delta t_n \mathbf{R}_0^\alpha : \dot{\bar{\boldsymbol{\sigma}}}(t_n); \\ \qquad\qquad = \tau^\alpha(t_n) + \delta t_n \mathbf{R}_0^\alpha : \bar{\mathbf{c}}^e : \left( \bar{\mathbf{d}}(t_n) - \sum\limits_{\beta\in\mathcal{P}} \dot{\gamma}^\beta(t_n)\mathbf{R}_0^\beta \right); \\ \tau_c^\alpha(t_{n+1}) = \tau_c^\alpha(t_n) + \delta t_n \dot{\tau}_c^\alpha(t_n) = \tau_c^\alpha(t_n) + \delta t_n \sum\limits_{\beta\in\mathcal{P}} H^{\alpha\beta}\dot{\gamma}^\beta(t_n). \end{cases} \tag{B.12}$$

The combination of Eqs. (B.11) and (B.12) provides the following minimization condition for $\delta t_n$:

$$\delta t_n = min_{\alpha\notin\mathcal{P}} \left\{ \Delta t, \frac{\tau_c^\alpha(t_n) - \tau^\alpha(t_n)}{\mathbf{R}_0^\alpha : \bar{\mathbf{c}}^e : \left( \bar{\mathbf{d}}(t_n) - \sum\limits_{\beta\in\mathcal{P}} \dot{\gamma}^\beta(t_n)\mathbf{R}_0^\beta \right) - \sum\limits_{\beta\in\mathcal{P}} H^{\alpha\beta}\dot{\gamma}^\beta(t_n)} \right\}. \tag{B.13}$$

Once the length $\delta t_n$ of the current sub-increment $\mathbf{I}^{\delta_n}$ determined, the other mechanical variables could be updated at $t_{n+1}$ as:

$$\begin{aligned}
&\delta\bar{\mathbf{r}}(t_n) = e^{\left( \delta t_n \left( \bar{\mathbf{w}}(t_n) - \sum\limits_{\alpha\in\mathcal{A}} \dot{\gamma}^\alpha(t_n)\mathbf{S}_0^\alpha \right) \right)}; \\
&\bar{\mathbf{r}}(t_{n+1}) = \bar{\mathbf{r}}(t_n) \cdot \delta\bar{\mathbf{r}}(t_n); \\
&\dot{\bar{\boldsymbol{\sigma}}}(t_n) = \bar{\mathbf{c}}^e : \left( \dot{\bar{\mathbf{d}}}(t_n) - \sum_{\alpha\in\mathcal{A}} \dot{\gamma}^\alpha(t_n)\mathbf{R}_0^\alpha \right); \\
&\bar{\boldsymbol{\sigma}}(t_{n+1}) = \bar{\boldsymbol{\sigma}}(t_n) + \delta t_n \dot{\bar{\boldsymbol{\sigma}}}(t_n); \\
&\boldsymbol{\sigma}(t_{n+1}) = \bar{\mathbf{r}}(t_{n+1}) \cdot \bar{\boldsymbol{\sigma}}(t_{n+1}) \cdot \bar{\mathbf{r}}^T(t_{n+1}); \\
&\forall \alpha \in 1, \dots, 2N_s \,:\, \begin{cases} \gamma^\alpha(t_{n+1}) = \gamma^\alpha(t_n) + \delta t_n \dot{\gamma}^\alpha(t_n); \\ \tau_c^\alpha(t_{n+1}) = \tau_c^\alpha(t_n) + \delta t_n \sum\limits_{\beta\in\mathcal{A}} H^{\alpha\beta}\dot{\gamma}^\beta(t_n). \end{cases}
\end{aligned} \tag{B.14}$$

The Cauchy stress tensor $\boldsymbol{\sigma}(t_{n+1})$ is computed by Eq. (B.14). It should be rotated in the co-rotational frame defined by rotation $\bar{\mathbf{r}}(t_{n+1})$, which is updated by Eq. (B.4), to obtain $\bar{\boldsymbol{\sigma}}(t_{n+1})$:

$$\bar{\boldsymbol{\sigma}}(t_{n+1}) = \bar{\mathbf{r}}^T(t_{n+1}) \cdot \boldsymbol{\sigma}(t_{n+1}) \cdot \bar{\mathbf{r}}(t_{n+1}). \tag{B.15}$$

Now, the consistent tangent modulus $\bar{\mathbf{c}}^{ep}$ should be determined. As the integration scheme is explicit, $\bar{\mathbf{c}}^{ep}$ can be obtained from the following relation between $\delta\bar{\boldsymbol{\sigma}}$ and $\delta\bar{\boldsymbol{\varepsilon}}$:

$$\delta\bar{\boldsymbol{\sigma}} = \bar{\mathbf{c}}^{ep} : \delta\bar{\boldsymbol{\varepsilon}}. \tag{B.16}$$

The stress sub-increment $\delta\bar{\boldsymbol{\sigma}}$ can be expressed as:

$$\begin{aligned}
\delta\bar{\boldsymbol{\sigma}} &= \bar{\boldsymbol{\sigma}}(t_{n+1}) - \bar{\boldsymbol{\sigma}}(t_n) = \hat{\mathbf{r}}^T(t_{n+1}) \cdot \boldsymbol{\sigma}(t_{n+1}) \cdot \hat{\mathbf{r}}(t_{n+1}) - \bar{\boldsymbol{\sigma}}(t_n); \\
&= \hat{\mathbf{r}}^T(t_{n+1}) \cdot \bar{\boldsymbol{\sigma}}(t_{n+1}) \cdot \hat{\mathbf{r}}(t_{n+1}) - \bar{\boldsymbol{\sigma}}(t_n),
\end{aligned} \tag{B.17}$$

where $\hat{\mathbf{r}}$ is the rotation of the intermediate configuration with respect to the co-rotational frame. This rotation is defined by the following evolution rule:

$$\hat{\mathbf{r}}(t_{n+1}) = \mathbf{e}^{-\delta t_n \hat{\mathbf{w}}^p(t_n)} \cdot \hat{\mathbf{r}}(t_n) = e^{-\delta t_n \sum\limits_{\alpha\in\mathcal{A}} \dot{\gamma}^\alpha(t_n)\hat{\mathbf{S}}^\alpha(t_n)} \cdot \hat{\mathbf{r}}(t_n). \tag{B.18}$$

Using Eq. (B.14), $\delta\tilde{\boldsymbol{\sigma}}$ can be rewritten as:

$$\begin{aligned}\delta\tilde{\boldsymbol{\sigma}} = \tilde{\boldsymbol{\sigma}}(t_{n+1}) - \tilde{\boldsymbol{\sigma}}(t_n) =& \hat{\mathbf{r}}(t_{n+1}) \cdot \left(\tilde{\boldsymbol{\sigma}}(t_n) + \delta t_n \dot{\tilde{\boldsymbol{\sigma}}}(t_n)\right) \cdot \hat{\mathbf{r}}^T(t_{n+1}) - \tilde{\boldsymbol{\sigma}}(t_n);\\ =& \left[\hat{\mathbf{r}}(t_{n+1}) \cdot \hat{\mathbf{r}}^T(t_n)\right] \cdot \tilde{\boldsymbol{\sigma}}(t_n) \cdot \left[\hat{\mathbf{r}}(t_{n+1}) \cdot \hat{\mathbf{r}}^T(t_n)\right]^T\\ &+ \delta t_n \hat{\mathbf{r}}(t_{n+1}) \cdot \dot{\tilde{\boldsymbol{\sigma}}}(t_n) \cdot \hat{\mathbf{r}}^T(t_{n+1}) - \tilde{\boldsymbol{\sigma}}(t_n).\end{aligned} \tag{B.19}$$

The expressions of $\left[\hat{\mathbf{r}}(t_{n+1}) \cdot \hat{\mathbf{r}}^T(t_n)\right]$ and $\left[\hat{\mathbf{r}}(t_{n+1}) \cdot \hat{\mathbf{r}}^T(t_n)\right]^T$ can be obtained from Eq. (B.18):

$$\hat{\mathbf{r}}(t_{n+1}) \cdot \hat{\mathbf{r}}^T(t_n) = e^{-\delta t_n \sum\limits_{\alpha\in\mathcal{A}} \dot{\gamma}^\alpha(t_n)\tilde{\mathbf{S}}^\alpha(t_n)}; \ \left[\hat{\mathbf{r}}(t_{n+1}) \cdot \hat{\mathbf{r}}^T(t_n)\right]^T = e^{\delta t_n \sum\limits_{\alpha\in\mathcal{A}} \dot{\gamma}^\alpha(t_n)\tilde{\mathbf{S}}^\alpha(t_n)}. \tag{B.20}$$

The Taylor expansion of tensors $e^{-\delta t_n \sum\limits_{\alpha\in\mathcal{A}} \dot{\gamma}^\alpha(t_n)\tilde{\mathbf{S}}^\alpha(t_n)}$ and $e^{\delta t_n \sum\limits_{\alpha\in\mathcal{A}} \dot{\gamma}^\alpha(t_n)\tilde{\mathbf{S}}^\alpha(t_n)}$ at the first order yields:

$$\begin{aligned}e^{-\delta t_n \sum\limits_{\alpha\in\mathcal{A}} \dot{\gamma}^\alpha(t_n)\tilde{\mathbf{S}}^\alpha(t_n)} &= \mathbf{I}_2 - \delta t_n \sum_{\alpha\in\mathcal{A}} \dot{\gamma}^\alpha(t_n)\tilde{\mathbf{S}}^\alpha(t_n);\\ e^{\delta t_n \sum\limits_{\alpha\in\mathcal{A}} \dot{\gamma}^\alpha(t_n)\tilde{\mathbf{S}}^\alpha(t_n)} &= \mathbf{I}_2 + \delta t_n \sum_{\alpha\in\mathcal{A}} \dot{\gamma}^\alpha(t_n)\tilde{\mathbf{S}}^\alpha(t_n).\end{aligned} \tag{B.21}$$

Considering the approximations Eq. (B.21), Eq. (B.19) can be recast to the following form:

$$\begin{aligned}\delta\tilde{\boldsymbol{\sigma}} = \tilde{\boldsymbol{\sigma}}(t_{n+1}) - \tilde{\boldsymbol{\sigma}}(t_n) =& \hat{\mathbf{r}}(t_{n+1}) \cdot \left(\tilde{\boldsymbol{\sigma}}(t_n) + \delta t_n \dot{\tilde{\boldsymbol{\sigma}}}(t_n)\right) \cdot \hat{\mathbf{r}}^T(t_{n+1}) - \tilde{\boldsymbol{\sigma}}(t_n);\\ =& \left[\mathbf{I}_2 - \delta t_n \sum_{\alpha\in\mathcal{A}} \dot{\gamma}^\alpha(t_n)\tilde{\mathbf{S}}^\alpha(t_n)\right] \cdot \tilde{\boldsymbol{\sigma}}(t_n)\\ &\cdot \left[\mathbf{I}_2 + \delta t_n \sum_{\alpha\in\mathcal{A}} \dot{\gamma}^\alpha(t_n)\tilde{\mathbf{S}}^\alpha(t_n)\right]\\ &+ \delta t_n \hat{\mathbf{r}}(t_{n+1}) \cdot \dot{\tilde{\boldsymbol{\sigma}}}(t_n) \cdot \hat{\mathbf{r}}^T(t_{n+1}) - \tilde{\boldsymbol{\sigma}}(t_n).\end{aligned} \tag{B.22}$$

Neglecting the second-order terms in $\delta t_n$, Eq. (B.22) can be reduced to the following form:

$$\begin{aligned}\delta\tilde{\boldsymbol{\sigma}} = \tilde{\boldsymbol{\sigma}}(t_{n+1}) - \tilde{\boldsymbol{\sigma}}(t_n) =& \hat{\mathbf{r}}(t_{n+1}) \cdot \left(\tilde{\boldsymbol{\sigma}}(t_n) + \delta t_n \dot{\tilde{\boldsymbol{\sigma}}}(t_n)\right) \cdot \hat{\mathbf{r}}^T(t_{n+1}) - \tilde{\boldsymbol{\sigma}}(t_n);\\ =& -\delta t_n \sum_{\alpha\in\mathcal{A}} \dot{\gamma}^\alpha(t_n)\tilde{\mathbf{S}}^\alpha(t_n) \cdot \tilde{\boldsymbol{\sigma}}(t_n)\\ &+ \delta t_n \tilde{\boldsymbol{\sigma}}(t_n) \cdot \sum_{\alpha\in\mathcal{A}} \dot{\gamma}^\alpha(t_n)\tilde{\mathbf{S}}^\alpha(t_n)\\ &+ \delta t_n \hat{\mathbf{r}}(t_{n+1}) \cdot \dot{\tilde{\boldsymbol{\sigma}}}(t_n) \cdot \hat{\mathbf{r}}^T(t_{n+1}).\end{aligned} \tag{B.23}$$

Tensor $\hat{\mathbf{r}}(t_{n+1}) \cdot \dot{\tilde{\boldsymbol{\sigma}}}(t_n) \cdot \hat{\mathbf{r}}^T(t_{n+1})$ can be expressed using Eq. (B.14) as:

$$\hat{\mathbf{r}}(t_{n+1}) \cdot \dot{\tilde{\boldsymbol{\sigma}}}(t_n) \cdot \hat{\mathbf{r}}^T(t_{n+1}) = \tilde{\mathbf{c}}^e : \left(\tilde{\mathbf{d}}(t_n) - \sum_{\alpha\in\mathcal{P}} \dot{\gamma}^\alpha(t_n)\tilde{\mathbf{R}}^\alpha_0(t_n)\right). \tag{B.24}$$

The analytical expression of the slip rates can be easily obtained from the combination of Eqs. (B.8) and (B.9):

$$\forall\alpha \in \mathcal{A} : \dot{\gamma}^\alpha(t_n) = \sum_{\beta\in\mathcal{A}} \Lambda^{\alpha\beta}\tilde{\mathbf{R}}^\beta(t_n) : \tilde{\mathbf{c}}^e : \tilde{\mathbf{d}}(t_n), \tag{B.25}$$

where the square matrix $\boldsymbol{\Lambda}(t_n)$ is the inverse of $\mathbf{A}(t_n)$, defined by index form in Eq. (B.8).

Taking into account expression Eq. (B.25) for $\dot{\gamma}^\alpha(t_n)$, Eq. (B.24) can be rewritten as:

$$\begin{aligned}&\hat{\mathbf{r}}(t_{n+1}) \cdot \dot{\tilde{\boldsymbol{\sigma}}}(t_n) \cdot \hat{\mathbf{r}}^T(t_{n+1})\\ &= \left[\tilde{\mathbf{c}}^e - \sum_{\alpha\in\mathcal{A}}\sum_{\beta\in\mathcal{A}} \Lambda^{\alpha\beta}(t_n)\left(\tilde{\mathbf{c}}^e : \tilde{\mathbf{R}}^\alpha(t_n)\right) \otimes \left(\tilde{\mathbf{R}}^\beta(t_n) : \tilde{\mathbf{c}}^e\right)\right] : \tilde{\mathbf{d}}(t_n).\end{aligned} \tag{B.26}$$

By inserting Eq. (B.26) into Eq. (B.23), and using expression Eq. (B.25), one obtains:

$$\begin{aligned}\delta\tilde{\boldsymbol{\sigma}} =& \delta t_n \left[\tilde{\mathbf{c}}^e - \sum_{\alpha\in\mathcal{A}}\sum_{\beta\in\mathcal{A}} \Lambda^{\alpha\beta}(t_n)\left(\tilde{\mathbf{c}}^e : \tilde{\mathbf{R}}^\alpha(t_n) + \tilde{\mathbf{S}}^\alpha(t_n) \cdot \tilde{\boldsymbol{\sigma}}(t_n)\right.\right.\\ &\left.\left. -\tilde{\boldsymbol{\sigma}}(t_n) \cdot \tilde{\mathbf{S}}^\alpha(t_n)\right) \otimes \left(\tilde{\mathbf{R}}^\beta(t_n) : \tilde{\mathbf{c}}^e\right)\right] : \tilde{\mathbf{d}}(t_n);\\ =& \left[\tilde{\mathbf{c}}^e - \sum_{\alpha\in\mathcal{A}}\sum_{\beta\in\mathcal{A}} \Lambda^{\alpha\beta}(t_n)\left(\tilde{\mathbf{c}}^e : \tilde{\mathbf{R}}^\alpha(t_n) + \tilde{\mathbf{S}}^\alpha(t_n) \cdot \tilde{\boldsymbol{\sigma}}(t_n)\right.\right.\\ &\left.\left. -\tilde{\boldsymbol{\sigma}}(t_n) \cdot \tilde{\mathbf{S}}^\alpha(t_n)\right) \otimes \left(\tilde{\mathbf{R}}^\beta(t_n) : \tilde{\mathbf{c}}^e\right)\right] : \delta\tilde{\boldsymbol{\varepsilon}}.\end{aligned} \tag{B.27}$$

The consistent tangent modulus $\tilde{\mathbf{c}}^{ep}$ can be thereby identified by comparing Eqs. (B.16) and (B.27):

$$\begin{aligned}\tilde{\mathbf{c}}^{ep} = \tilde{\mathbf{c}}^e - \sum_{\alpha\in\mathcal{A}}\sum_{\beta\in\mathcal{A}} \Lambda^{\alpha\beta}(t_n)\left(\tilde{\mathbf{c}}^e : \tilde{\mathbf{R}}^\alpha(t_n) + \tilde{\mathbf{S}}^\alpha(t_n) \cdot \tilde{\boldsymbol{\sigma}}(t_n)\right.\\ \left. -\tilde{\boldsymbol{\sigma}}(t_n) \cdot \tilde{\mathbf{S}}^\alpha(t_n)\right) \otimes \left(\tilde{\mathbf{R}}^\beta(t_n) : \tilde{\mathbf{c}}^e\right).\end{aligned} \tag{B.28}$$

Once all the mechanical variables updated at $t_{n+1}$, and the consistent tangent modulus $\tilde{\mathbf{c}}^{ep}$ computed, the size of the time increment $\Delta t$ and the initial time $t_n$ should be also updated:

$$\Delta t \leftarrow \Delta t - \delta t_n; \ t_n \leftarrow t_n + \delta t_n. \tag{B.29}$$

After this update procedure, the computation should be restarted with a new sub-increment $\mathbf{I}^{\delta_n}$, until reaching the following condition:

$$\Delta t = \delta t_n. \tag{B.30}$$

## References


ABAQUS, 2014. User's Manual 6.14. Abaqus Inc..

Adam, K., Zöllner, D., Field, D.P., 2018. 3D microstructural evolution of primary recrystallization and grain growth in cold rolled single-phase aluminum alloys. Modelling Simul. Mater. Sci. Eng. 26 (3), http://dx.doi.org/10.1088/1361-651X/aaa146.

Akpama, H.K., Ben Bettaieb, M., Abed-Meraim, F., 2016. Numerical integration of rate-independent BCC single crystal plasticity models: comparative study of two classes of numerical algorithms. Internat. J. Numer. Methods Engrg. 108 (5), 363–422. http://dx.doi.org/10.1002/nme.5215.

Akpama, H.K., Ben Bettaieb, M., Abed-Meraim, F., 2017. Localized necking predictions based on rate-independent self-consistent polycrystal plasticity: Bifurcation analysis versus imperfection approach. Int. J. Plast. 91, 205–237. http://dx.doi.org/10.1016/j.ijplas.2017.02.001.

Amelirad, O., Assempour, A., 2019. Experimental and crystal plasticity evaluation of grain size effect on formability of austenitic stainless steel sheets. J. Manuf. Process. 47, 310–323. http://dx.doi.org/10.1016/j.jmapro.2019.09.035.

Anand, L., Kothari, M., 1996. A computational procedure for rate-independent crystal plasticity. J. Mech. Phys. Solids 44 (4), 525–558. http://dx.doi.org/10.1016/0022-5096(96)00001-4.

Barlat, F., 1987. Crystallographic texture, anisotropic yield surfaces and forming limits of sheet metals. Mater. Sci. Eng. 91, 55–72. http://dx.doi.org/10.1016/0025-5416(87)90283-7.

Beausir, B., Fundenberger, J.-J., 2017. Analysis tools for electron and X-ray diffraction, ATEX - software. www.atex-software.eu.

Ben Bettaieb, M., Abed-Meraim, F., 2015. Investigation of localized necking in substrate-supported metal layers: Comparison of bifurcation and imperfection analyses. Int. J. Plast. 65, 168–190. http://dx.doi.org/10.1016/j.ijplas.2014.09.003.

Ben Bettaieb, M., Abed-Meraim, F., 2017a. Effect of kinematic hardening on localized necking in substrate-supported metal layers. Int. J. Mech. Sci. 123, 177–197. http://dx.doi.org/10.1016/j.ijmecsci.2016.12.002.

Ben Bettaieb, M., Abed-Meraim, F., 2017b. Strain rate effects on localized necking in substrate-supported metal layers. Int. J. Adv. Manuf. Technol. 92 (9), 3461–3480. http://dx.doi.org/10.1007/s00170-017-0344-8.

Ben Bettaieb, M., Abed-Meraim, F., 2021. Formability prediction of substrate-supported metal layers using a non-associated plastic flow rule. J. Mater Process. Technol. 287, 116694. http://dx.doi.org/10.1016/j.jmatprotec.2020.116694.

Ben Bettaieb, M., Débordes, O., Dogui, A., Duchêne, L., 2012. Averaging properties for periodic homogenization and large deformation. Int. J. Multiscale Comput. Eng. 10 (3), http://dx.doi.org/10.1615/IntJMultCompEng.2012002587.

Ben Bettaieb, M., Débordes, O., Dogui, A., Duchêne, L., Keller, C., 2012. On the numerical integration of rate independent single crystal behavior at large strain. Int. J. Plast. 32–33, 184–217. http://dx.doi.org/10.1016/j.ijplas.2011.10.010.

Borja, R.I., Wren, J.R., 1993. Discrete micromechanics of elastoplastic crystals. Internat. J. Numer. Methods Engrg. 36 (22), 3815–3840. http://dx.doi.org/10.1002/nme.1620362205.

Butuc, M.C., Barlat, F., Vincze, G., 2021. The formability of twinning-Induced plasticity steels predicted on the base of Marciniak-Kuczynski theory. J. Mater Process. Technol. 287, 116496. http://dx.doi.org/10.1016/j.jmatprotec.2019.116496.

Chandola, N., Cazacu, O., Revil-Baudard, B., 2018. Prediction of plastic anisotropy of textured polycrystalline sheets using a new single-crystal model. Compt. R. - Mec. 346 (8), 756–769. http://dx.doi.org/10.1016/j.crme.2018.05.004.

Chaugule, P.S., le Graverend, J.-B., 2022. Crystal-plasticity modeling of phase transformation-viscoplasticity coupling in high-temperature shape memory alloys. Int. J. Plast. 153, 103243. http://dx.doi.org/10.1016/j.ijplas.2022.103243.

Considère, M., 1885. Memoire Sur L'emploi Du Fer Et De L'acier Dans Les Constructions. Ch. Dunod, Editeur.

Farhat, Z.N., Ding, Y., Northwood, D.O., Alpas, A.T., 1996. Effect of grain size on friction and wear of nanocrystalline aluminum. Mater. Sci. Eng. A 206 (2), 302–313. http://dx.doi.org/10.1016/0921-5093(95)10016-4.

Franz, G., Abed-Meraim, F., Berveiller, M., 2013. Strain localization analysis for single crystals and polycrystals: Towards microstructure-ductility linkage. Int. J. Plast. 48, 1–33. http://dx.doi.org/10.1016/j.ijplas.2013.02.001.

Gau, J.T., Principe, C., Wang, J., 2007. An experimental study on size effects on flow stress and formability of aluminm and brass for microforming. J. Mater Process. Technol. 184 (1–3), 42–46. http://dx.doi.org/10.1016/j.jmatprotec.2006.11.003.

Goodwin, G.M., 1968. Application of strain analysis to sheet metal forming problems in the press shop. SAE Tech. Pap. 380–387. http://dx.doi.org/10.4271/680093.

Gupta, A., Ben Bettaieb, M., Abed-Meraim, F., Kalidindi, S.R., 2018. Computationally efficient predictions of crystal plasticity based forming limit diagrams using a spectral database. Int. J. Plast. 103, 168–187. http://dx.doi.org/10.1016/j.ijplas.2018.01.007.

Haddag, B., Abed-Meraim, F., Balan, T., 2009. Strain localization analysis using a large deformation anisotropic elastic-plastic model coupled with damage. Int. J. Plast. 25 (10), 1970–1996. http://dx.doi.org/10.1016/j.ijplas.2008.12.013.

Helming, K., Schwarzer, R., Rauschenbach, B., Geier, S., Leiss, B., Wenk, H., Ullemeyer, K., Heinitz, J., 1994. Texture estimates by means of components. Z. Fur Met. 85 (8), 545–553.

Inal, K., Neale, K.W., Aboutajeddine, A., 2005. Forming limit comparisons for FCC and BCC sheets. Int. J. Plast. 21 (6), 1255–1266. http://dx.doi.org/10.1016/j.ijplas.2004.08.001.

Jedidi, M.Y., Ben Bettaieb, M., Abed-Meraim, F., Khabou, M.T., Bouguecha, A., Haddar, M., 2020. Prediction of necking in HCP sheet metals using a two-surface plasticity model. Int. J. Plast. 128, 102641. http://dx.doi.org/10.1016/j.ijplas.2019.102641.

Jeong, Y., Barlat, F., Tomé, C.N., Wen, W., 2017. A comparative study between micro- and macro-mechanical constitutive models developed for complex loading scenarios. Int. J. Plast. 93, 212–228. http://dx.doi.org/10.1016/j.ijplas.2016.07.015.

Jeong, J., Voyiadjis, G.Z., 2022. A physics-based crystal plasticity model for the prediction of the dislocation densities in micropillar compression. J. Mech. Phys. Solids 167, 105006. http://dx.doi.org/10.1016/j.jmps.2022.105006.

Kanjarla, A.K., Van Houtte, P., Delannay, L., 2010. Assessment of plastic heterogeneity in grain interaction models using crystal plasticity finite element method. Int. J. Plast. 26 (8), 1220–1233. http://dx.doi.org/10.1016/j.ijplas.2009.05.005.

Keeler, S.P., Backhofen, W.A., 1963. Plastic instability and fracture in sheets stretched over rigid punches. ASM Trans. Q. 56, 25–48.

Kim, J.H., Lee, M.-G., Kang, J.-H., Oh, C.-S., Barlat, F., 2017. Crystal plasticity finite element analysis of ferritic stainless steel for sheet formability prediction. Int. J. Plast. 93, 26–45. http://dx.doi.org/10.1016/j.ijplas.2017.04.007.

Knockaert, R., Chastel, Y., Massoni, E., 2002. Forming limits prediction using rate-independent polycrystalline plasticity. Int. J. Plast. 18 (2), 231–247. http://dx.doi.org/10.1016/S0749-6419(00)00077-2.

Kuroda, M., 2005. Effects of texture on mechanical properties of aluminum alloy sheets and texture optimization strategy. AIP Conf. Proc. 778 A, 445–450. http://dx.doi.org/10.1063/1.2011260.

Kuroda, M., 2007. Effects of crystallographic texture on plastic flow localization. Key Eng. Mater. 340–341, 211–216. http://dx.doi.org/10.4028/www.scientific.net/kem.340-341.211.

Lejeunes, S., Bourgeois, S., 2011. Une Toolbox Abaqus pour le calcul de propriétés effectives de milieux hétérogènes. In: 10e Colloq. Natl. en Calc. des Struct.. Giens, France, pp. 1–9.

Lévesque, J., Inal, K., Neale, K.W., Mishra, R.K., 2010. Numerical modeling of formability of extruded magnesium alloy tubes. Int. J. Plast. 26 (1), 65–83. http://dx.doi.org/10.1016/j.ijplas.2009.05.001.

Lim, H., Battaile, C.C., Bishop, J.E., Foulk, J.W., 2019. Investigating mesh sensitivity and polycrystalline RVEs in crystal plasticity finite element simulations. Int. J. Plast. 121, 101–115. http://dx.doi.org/10.1016/j.ijplas.2019.06.001.

Ma, B., Diao, K., Wu, X., Li, X., Wan, M., Cai, Z., 2016. The effect of the through-thickness normal stress on sheet formability. J. Manuf. Process. 21, 134–140. http://dx.doi.org/10.1016/j.jmapro.2015.12.006.

Manopulo, N., Hora, P., Peters, P., Gorji, M., Barlat, F., 2015. An extended modified maximum force criterion for the prediction of localized necking under non-proportional loading. Int. J. Plast. 75, 189–203. http://dx.doi.org/10.1016/j.ijplas.2015.02.003.

Mansouri, L.Z., Chalal, H., Abed-Meraim, F., 2014. Ductility limit prediction using a GTN damage model coupled with localization bifurcation analysis. Mech. Mater. 76, 64–92. http://dx.doi.org/10.1016/j.mechmat.2014.06.005.

Marciniak, Z., Kuczyński, K., 1967. Limit strains in the processes of stretch-forming sheet metal. Int. J. Mech. Sci. 9 (9), 609–620. http://dx.doi.org/10.1016/0020-7403(67)90066-5.

Nagra, J.S., Brahme, A., Lévesque, J., Mishra, R., Lebensohn, R.A., Inal, K., 2020. A new micromechanics based full field numerical framework to simulate the effects of dynamic recrystallization on the formability of HCP metals. Int. J. Plast. 125, 210–234. http://dx.doi.org/10.1016/j.ijplas.2019.09.011.

Nagra, J.S., Brahme, A., Mishra, R., Lebensohn, R.A., Inal, K., 2018. An efficient full-field crystal plasticity-based M–K framework to study the effect of 3D microstructural features on the formability of polycrystalline materials. Modelling Simul. Mater. Sci. Eng. 26 (7), 75002. http://dx.doi.org/10.1088/1361-651x/aadc20.

Nakamachi, E., Xie, C.L., Morimoto, H., Morita, K., Yokoyama, N., 2002. Formability assessment of FCC aluminum alloy sheet by using elastic/crystalline viscoplastic finite element analysis. Int. J. Plast. 18 (5–6), 617–632. http://dx.doi.org/10.1016/S0749-6419(01)00052-3.

Onimus, F., Gélébart, L., Brenner, R., 2022. Polycrystalline simulations of in-reactor deformation of recrystallized Zircaloy-4 tubes: Fast Fourier Transform computations and mean-field self-consistent model. Int. J. Plast. 153, 103272. http://dx.doi.org/10.1016/j.ijplas.2022.103272.

Patil, C.S., Chakraborty, S., Niezgoda, S.R., 2021. Comparison of full field predictions of crystal plasticity simulations using the voce and the dislocation density based hardening laws. Int. J. Plast. 147, 103099. http://dx.doi.org/10.1016/j.ijplas.2021.103099.

Quey, R., Dawson, P.R., Barbe, F., 2011. Large-scale 3D random polycrystals for the finite element method: Generation, meshing and remeshing. Comput. Methods Appl. Mech. Engrg. 200 (17), 1729–1745. http://dx.doi.org/10.1016/j.cma.2011.01.002.

Raabe, D., Roters, F., 2004. Using texture components in crystal plasticity finite element simulations. Int. J. Plast. 20 (3), 339–361. http://dx.doi.org/10.1016/S0749-6419(03)00092-5.

Rice, J., 1976. The localization of plastic deformation. In: 14th International Congress of Theoretical and Applied Mechanics. pp. 207–220.

Rudnicki, J.W., Rice, J.R., 1975. Conditions for the localization of deformation in pressure-sensitive dilatant materials. J. Mech. Phys. Solids 23 (6), 371–394. http://dx.doi.org/10.1016/0022-5096(75)90001-0.

Schmid, E., Boas, W., 1935. Plasticity of Crystals. Chapman and Hall, London.

Schwindt, C., Schlosser, F., Bertinetti, M.A., Stout, M., Signorelli, J.W., 2015. Experimental and Visco-Plastic Self-Consistent evaluation of forming limit diagrams for anisotropic sheet metals: An efficient and robust implementation of the M-K model. Int. J. Plast. 73, 62–99. http://dx.doi.org/10.1016/j.ijplas.2015.01.005.

Signorelli, J.W., Bertinetti, M.A., Roatta, A., 2021. A review of recent investigations using the Marciniak-Kuczynski technique in conjunction with crystal plasticity models. J. Mater Process. Technol. 287, 116517. http://dx.doi.org/10.1016/j.jmatprotec.2019.116517.

Signorelli, J.W., Bertinetti, M.A., Turner, P.A., 2009. Predictions of forming limit diagrams using a rate-dependent polycrystal self-consistent plasticity model. Int. J. Plast. 25 (1), 1–25. http://dx.doi.org/10.1016/j.ijplas.2008.01.005.

Swift, H.W., 1952. Plastic instability under plane stress. J. Mech. Phys. Solids 1 (1), 1–18. http://dx.doi.org/10.1016/0022-5096(52)90002-1.

Tadano, Y., Yoshida, K., Kuroda, M., 2013. Plastic flow localization analysis of heterogeneous materials using homogenization-based finite element method. Int. J. Mech. Sci. 72, 63–74. http://dx.doi.org/10.1016/j.ijmecsci.2013.03.015.

Tran, M.T., Wang, H., Lee, H.W., Kim, D.-K., 2022. Crystal plasticity finite element analysis of size effect on the formability of ultra-thin ferritic stainless steel sheet for fuel cell bipolar plate. Int. J. Plast. 154, 103298. http://dx.doi.org/10.1016/j.ijplas.2022.103298.

Wu, P.D., Lloyd, D.J., Jain, M., Neale, K.W., Huang, Y., 2007. Effects of spatial grain orientation distribution and initial surface topography on sheet metal necking. Int. J. Plast. 23 (6), 1084–1104. http://dx.doi.org/10.1016/j.ijplas.2006.11.005.

Xu, Z.T., Peng, L.F., Fu, M.W., Lai, X.M., 2015. Size effect affected formability of sheet metals in micro/meso scale plastic deformation: Experiment and modeling. Int. J. Plast. 68, 34–54. http://dx.doi.org/10.1016/j.ijplas.2014.11.002.

Xu, Z.T., Peng, L.F., Lai, X.M., Fu, M.W., 2014. Geometry and grain size effects on the forming limit of sheet metals in micro-scaled plastic deformation. Mater. Sci. Eng. A 611, 345–353. http://dx.doi.org/10.1016/j.msea.2014.05.060.

Yoshida, K., Ishizaka, T., Kuroda, M., Ikawa, S., 2007. The effects of texture on formability of aluminum alloy sheets. Acta Mater. 55 (13), 4499–4506. http://dx.doi.org/10.1016/j.actamat.2007.04.014.

Yoshida, K., Kuroda, M., 2012. Comparison of bifurcation and imperfection analyses of localized necking in rate-independent polycrystalline sheets. Int. J. Solids Struct. 49 (15–16), 2073–2084. http://dx.doi.org/10.1016/j.ijsolstr.2012.04.010.

Zhang, H., Liu, J., Sui, D., Cui, Z., Fu, M.W., 2018. Study of microstructural grain and geometric size effects on plastic heterogeneities at grain-level by using crystal plasticity modeling with high-fidelity representative microstructures. Int. J. Plast. 100, 69–89. http://dx.doi.org/10.1016/j.ijplas.2017.09.011.

Zhang, X., Zhao, J., Kang, G., Zaiser, M., 2023. Geometrically necessary dislocations and related kinematic hardening in gradient grained materials: A nonlocal crystal plasticity study. Int. J. Plast. 163, 103553. http://dx.doi.org/10.1016/j.ijplas.2023.103553.

Zhou, R., Roy, A., Silberschmidt, V.V., 2019. A crystal-plasticity model of extruded AM30 magnesium alloy. Comput. Mater. Sci. 170, 109140. http://dx.doi.org/10.1016/j.commatsci.2019.109140.

Zhu, J.C., Ben Bettaieb, M., Abed-Meraim, F., 2020a. Investigation of the competition between void coalescence and macroscopic strain localization using the periodic homogenization multiscale scheme. J. Mech. Phys. Solids 143, 104042. http://dx.doi.org/10.1016/j.jmps.2020.104042.

Zhu, J.C., Ben Bettaieb, M., Abed-Meraim, F., 2020b. Numerical investigation of necking in perforated sheets using the periodic homogenization approach. Int. J. Mech. Sci. 166, http://dx.doi.org/10.1016/j.ijmecsci.2019.105209.

Zhu, J.C., Ben Bettaieb, M., Abed-Meraim, F., 2022. Comparative study of three techniques for the computation of the macroscopic tangent moduli by periodic homogenization scheme. Eng. Comput. 38, 1365–1394. http://dx.doi.org/10.1007/s00366-020-01091-y.

Zhu, J.C., Ben Bettaieb, M., Zhou, S., Abed-Meraim, F., 2023. Ductility limit prediction for polycrystalline aggregates using a CPFEM-based multiscale framework. Int. J. Plast. 167, 103671. http://dx.doi.org/10.1016/j.ijplas.2023.103671.